Geophysical Journal International

Geophys. J. Int. (2022) **230,** 1197–1214
Advance Access publication 2022 March 17
GJI Seismology

https://doi.org/10.1093/gji/ggac107

Highly heterogeneous upper-mantle structure in Fennoscandia from finite-frequency *P*-body-wave tomography

N. Bulut [1], H. Thybo [1,2,3] and V. Maupin [4]

[1] *Eurasia Institute of Earth Sciences, Istanbul Technical University, Maslak* 34469, *Istanbul, Turkey. E-mail: bulutne@itu.edu.tr ; h.thybo@gmail.com*
[2] *State Key Laboratory GPMR, School of Earth Sciences, China University of Geosciences, Wuhan* 430074, *China*
[3] *Sinoprobe Laboratory, Chinese Academy of Geological Sciences, Beijing* 100037, *China*
[4] *Center for Earth Evolution and Dynamics, University of Oslo, Blindern,* 0316 *Oslo, Norway*

Accepted 2022 March 15. Received 2022 March 7; in original form 2021 July 17

SUMMARY

We present a *P*-wave velocity model of the upper mantle, obtained from finite-frequency body-wave tomography, to analyse the relationship between deep and surface structures in Fennoscandia, one of the most studied cratons on the Earth. The large array aperture of 2000 km × 800 km allows us to image the velocity structure to 800 km depth at very high resolution. The velocity structure provides background for understanding the mechanisms responsible for the enigmatic and strongly debated high topography in the Scandinavian mountain range far from any plate boundary. Our model shows exceptionally strong velocity anomalies with changes by up to 6 per cent on a 200 km scale. We propose that a strong negative velocity anomaly down to 200 km depth along all of Norway provides isostatic support to the enigmatic topography, as we observe a linear correlation between hypsometry and uppermost mantle velocity anomalies to 150 km depth in central Fennoscandia. The model reveals a low-velocity anomaly below the mountains underlain by positive velocity anomalies, which we explain by preserved original Svecofennian and Archaean mantle below the Caledonian/Sveconorwegian deformed parts of Fennoscandia. Strong positive velocity anomalies to around 200 km depth around the southern Bothnian Bay and the Baltic Sea may be associated with pristine lithosphere of the present central and southern Fennoscandian craton that has been protected from modification since its formation. However, the Archaean domain in the north and the marginal parts of the Svecofennian domains appear to have experienced strong modification of the upper mantle. A pronounced north-dipping positive velocity anomaly in the southern Baltic Sea extends below Moho. It coincides in location and dip with a similar north-dipping structure in the crust and uppermost mantle to 80 km depth observed from high-resolution, controlled source seismic data. We interpret this feature as the image of a Palaeoproterozoic boundary that has been preserved for 1.8 Gy in the lithosphere.

Key words: Mantle processes; Body waves; Seismic tomography; Cratons; Dynamics of lithosphere and mantle.

1 INTRODUCTION

Fennoscandia is one of the geologically best studied cratons on the Earth and it provides an exceptional opportunity for studying the relationship between deep and surface structures. The craton is bounded by a more than 2000 km long, high mountain chain along its coastline to the North Atlantic Ocean, far from any plate boundary. Several studies describe widespread regional onshore uplift and offshore subsidence around the North Atlantic passive margins near the coasts of Greenland, British isles and Scandinavia (Japsen & Chalmers 2000; Anell *et al.* 2009, 2010, and references therein). Two end-member explanations have been proposed for the origin of this high topography: (1) It is old and has existed since the Palaeozoic Caledonian orogeny (Nielsen *et al.* 2009) and (2) it is young and caused by Mesozoic to Cenozoic surface and deep thermal or other geodynamic processes (Gabrielsen *et al.* 2010).

Understanding the mechanisms behind the high and recent topography around the North Atlantic Ocean and its relation to geodynamic processes requires knowledge of the deep lithospheric structure. This study provides new evidence for the upper mantle structure in Fennoscandia based on a tomographic inversion of teleseismic arrivals (Fig. 1). Our new model of the *P*-wave seismic velocity structure down to a depth of 800 km is derived by finite-frequency body-wave tomography based on traveltime residuals. It

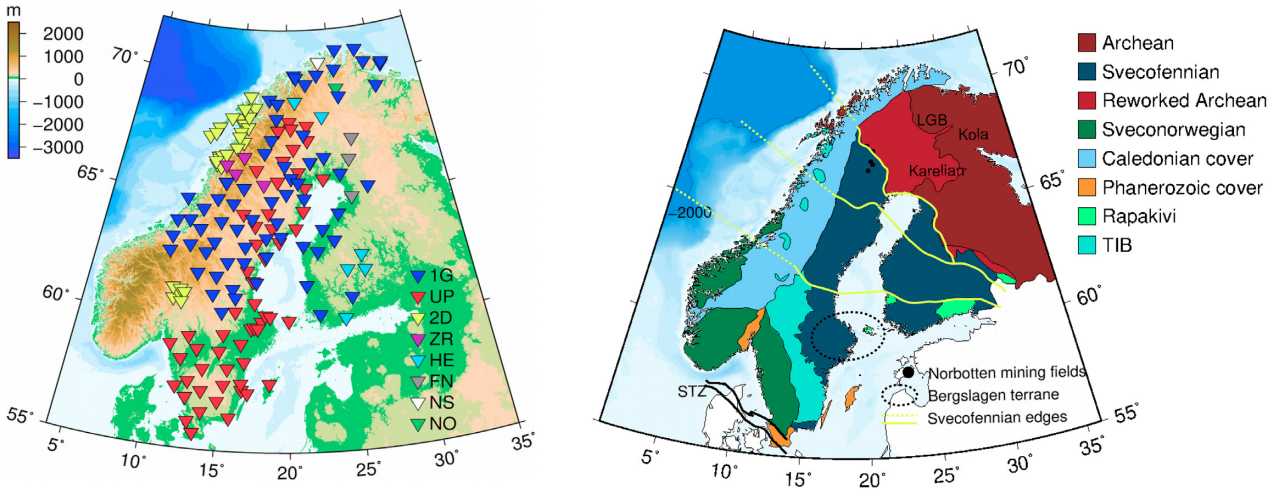

Figure 1. Station network and surface geology in the region. Left-hand panel: Hypsometry map of Scandinavia and the location of seismic stations used in this study; coloured triangles represent different networks. Right-hand panel: Simplified geological units of Fennoscandia (after Gaal & Gorbatschev 1987). TIB: Transscandinavian Igneous Belt. STZ: Sorgenfrei-Tornquist zone. LGB: Lapland Granulite Belt. The −2000 m bathymetry contour with a thin solid line roughly represents the outer margin of the Vøring Plateau.

provides a basis for inferring high resolution models of temperature and compositional anomalies that may contribute to understanding the mechanisms responsible for the enigmatic topography in the framework of the general tectonic and geological evolution of the North Atlantic region. It may further enlighten the connection between deep lithospheric structure and surface/crustal geology and contribute to the ongoing discussion about whether the lithospheric crust and mantle have evolved as a single unit since formation or they may have been subject to different tectonic or other dynamic processes.

2 TECTONIC SETTINGS

Fennoscandia is the northwestern part of the East European Craton formed by the Baltic Shield with a partial cover of remnant nappes of the Caledonide orogen in the western part (Fig. 1). The Baltic Shield includes an Archaean part in the northeast to which a series of continents and terranes amalgamated in the Proterozoic during the Svecofennian orogeny (Lahtinen *et al.* 2005) in three phases, which formed the northern, central, and southern Svecofennian domains (Gaal & Gorbatschev 1987). The Bergslagen arc and terrane are part of the Svecofennian orogen. The Transscandinavian Igneous Belt intruded large parts of the presently exposed Svecofennian provinces, including Bergslagen, and it includes significant ore deposits in south-central Sweden (Högdahl *et al.* 2004). Subsequently, the Sveconorwegian (Grenvillian) orogeny (Bingen *et al.* 2005, 2006) mainly affected the existing crust in Fennoscandia by reworking rather than adding new crust by amalgamation (Gaal & Gorbatschev 1987; Bingen *et al.* 2008).

The present Baltic Shield includes most of the former Baltica plate, which broke up from the Late Proterozoic supercontinent Rodinia (Torsvik *et al.* 1996). The collision between Baltica and Laurentia after the closure of the Iapetus Ocean in the mid-Palaeozoic resulted in the major Caledonian orogeny, as today observed in a nappe series in western Fennoscandia, which provides a relatively thin cover of the older basement (Gee *et al.* 2008). At approximately the same time, the closure of the Tornquist Ocean in the south resulted in the amalgamation of a series of unknown terranes termed Avalonia (Winchester *et al.* 2002).

Oceanic breakup around 60 Ma formed the North Atlantic Ocean within the Caledonian suture zone after a very long extensional period of over 200 My (Ziegler & Cloetingh 2004). The breakup was accompanied by extensive magmatism in the North Atlantic Igneous Province (NAIP), with major volcanic activity in east-central Greenland and around the Faroe Islands. It has been proposed that a mantle plume corresponding to the Iceland hotspot was centered beneath Greenland during the opening phase of the northeast Atlantic (Lawver & Müller 1994), but this interpretation has later been questioned (Torsvik *et al.* 2015). The breakup led to the formation of wide, submerged continental shelves on both sides of the North Atlantic Ocean along the coasts of Norway and Greenland (Japsen & Chalmers 2000; Anell *et al.* 2009 and references therein).

The present Scandinavian mountain range (Scandes) is primarily located in Caledonian deformed areas. It extends over two thousand km along the coast of Norway, with the highest elevation reaching ca. 2500 m in the southern Scandes. Similar high topography is found along the coast of Greenland on the other side of the North Atlantic Ocean. This high topography along the passive continental margins far from any plate boundary is enigmatic. The proposal that it represents remnant topography of the 444 Ma Caledonian orogeny (Nielsen *et al.* 2009; Pedersen *et al.* 2016) contradicts similar high topography observed at the conjugate margin in areas of Greenland. Here, high topography areas unaffected by the Caledonian orogeny include Jurassic marine sedimentary strata presently uplifted to around 1000 m (Surlyk 2003; Kraft *et al.* 2019 and references therein) and a Cenozoic volcanic province in central-eastern Greenland with peaks reaching more than 3000 m altitudes (Brooks 2011) as well as elevated Precambrian sequences in the southeast (Henriksen 2008).

A whole series of processes may have influenced the recent topographic change in the region, including onshore uplift and offshore subsidence on the shelves. Proposed mechanisms include uplift caused by the Iceland hotspot (Foulger & Pearson 2001; Marquart & Schmeling 2004) or local uplift by smaller 'hot fingers' from Iceland extending into the onshore parts (Weidle & Maupin 2008; Parnell-Turner *et al.* 2014; Shoonman *et al.* 2017), underplating in connection with magmatic activity (Molnar & Houseman 2004; Sandrin & Thybo 2008b; Mansour *et al.* 2018), mantle convection at

sharp changes in lithospheric thickness at the continental margins (King & Anderson 1998a), or stress from ridge push released at the ocean-to-continent lithospheric transition (Marotta *et al.* 2001; Cloetingh & Burov 2011). In addition, a series of other possible processes have been proposed. We refer to Anell *et al.* (2009) for an extensive list of processes based on a review of published observations of hypsometric change in the North Atlantic region.

It is characteristic that the crust is relatively thin below the southern Norwegian mountain range, with only minor thickening inland from the coastline (Stratford *et al.* 2009). However, the crustal thickness and structure change significantly from the Norwegian mountains to the Baltic Shield in Sweden. Crustal thickness is generally 30–35 km in Norway and up to 50 km in Sweden (Artemieva & Thybo 2013). The crust in Norway lacks a high-velocity lower crust, which is a characteristic of the cratonic lithosphere. The southern Norwegian mountains lack sufficient crustal roots to support the high topography by crustal isostasy (Anell *et al.* 2010). Moreover, it is suggested that the asymmetric topography (Medhus *et al.* 2012; Maupin *et al.* 2013) is supported by flexural bending of the lithosphere (England & Ebbing 2012). A relatively thin crust observed below the highest topography may indicate earlier delamination of a crustal or lithospheric root (Artemieva & Meissner 2012; Frassetto & Thybo 2013). Although the Neogene uplift in the northern Norwegian mountains has been less studied than its southern part, Ebbing & Olesen (2005) suggest that glacial erosion created the uplift rather than mantle processes. Isostatic support of the mountain range without crustal roots is possible because the average crustal density may change due to lateral changes in the lower crustal structure as well as lateral changes in the density of the lithospheric mantle. However, Anell *et al.* (2010) estimate that other processes than isostasy must support at least 30 per cent of the current topography in the southern dome. Seismic and gravity studies indicate that an abrupt thickening of the lithosphere between southern Norway and Sweden (Gradmann *et al.* 2013) is compatible with a depleted mantle composition below southern Sweden (e.g. Andersen & Sundvoll 1995; Artemieva 2003). The high topography in southern Norway may also be explained by a combination of Airy and Pratt isostasy (Frassetto & Thybo 2013). Maupin *et al.* (2013) find that low upper mantle velocity in southern Norway may extend deep into the mantle, but Makushkina *et al.* (2019) demonstrate by a high resolution receiver function study that the transition zone discontinuities at depths of 410 and 660 km are flat within the uncertainty range of 5–15 km. Therefore, the high topography in western Scandinavia cannot be related to a deep thermal anomaly.

3 DATA AND METHODS

3.1 Data

The ScanArray experiment (Thybo *et al.* 2012, 2021) is an extensive collaboration between the universities of Aarhus, Bergen, Copenhagen, Karlsruhe, Leicester, Oslo and Uppsala, Istanbul Technical University, GFZ Potsdam and NORSAR that focuses on the structure of the lithosphere and upper-mantle processes below Scandinavia. The experiment has acquired broad-band seismic data on a dense array of temporary seismometers for 4 yr. These data are subject to interpretation and inversion, by a wide variety of seismological methods. Seventy stations were dedicated to the core ScanArray project. We also use data from other stations belonging to permanent and temporary installations by the networks SNSN (59 stations), ScanLips3D (5 stations), NORSAR (8 stations), University of Helsinki (6 stations), University of Oulu (3 stations), Neonor (22 stations) and NNSN (1 station). We do not include data from stations belonging to previous nearby temporary experiments that did not overlap in time with the Scanarray network. Although some authors (e.g. Youssof *et al.* 2015) have combined data from different acquisition periods by ensuring that several stations recorded during both acquisition periods, there have been concerns if such procedure may introduce biases that potentially may invalidate the models (Maupin 2021). In total, we use data from 174 three-component broad-band seismic stations that operated during variable periods between 2012 and 2017 in Norway, Sweden, and Finland (Fig. 1). *P*-wave phases are gathered from teleseismic earthquakes at epicentral distances between 30° and 100° with magnitudes above 5.5 (Fig. 2). The large aperture of 2000 km × 800 km resolves the velocity structure down to 800 km depth throughout most of Fennoscandia.

3.2 Relative traveltime picking and relative traveltime residuals

Since the quality of the tomographic model directly depends on the precision of the traveltime residuals, it is crucial to measure accurate relative traveltimes. Therefore, we apply the data processing routine suggested by Kolstrup & Maupin (2015) to estimate the frequency-dependent traveltime residuals after correction for the effects of the crustal structure. We measure the traveltimes in two relatively narrow frequency bands since the propagation characteristics of seismic waves are frequency-dependent (Dahlen *et al.* 2000; Hung *et al.* 2001). The applied method minimizes the effects of uncertainties regarding exact source location, source origin time, and absolute velocity information.

After resampling to a common sampling rate and correction for instrument response, the procedure for estimating the residual traveltimes consists of five main steps:

(1) The seismograms are windowed around theoretical arrival times calculated by the *taup* Matlab program (Crotwell & Owens 1999) for the spherically symmetric, continental, one-dimensional Earth velocity model ak135 (Kennett 1995). A zero phase Butterworth filter is applied for the desired frequency ranges for all three components. High- and low-frequency bands used in this study are 0.5–2 Hz (2–0.5 s) and 0.03–0.125 Hz (33–8 s). These frequency ranges are the same as used by Kolstrup & Maupin (2015).

(2) The quality of the data is checked for noise level and possible station malfunction. Traces are rejected if the maximum envelope is eight times larger or ten times smaller than the median of all envelope maxima for a particular event. After each rejection, the median is updated until no more outliers are found in the data set.

(3) Smaller frequency-dependent time windows of data are selected around the expected arrival time of the phase under study. The lengths of the time windows are 42 and 16 s with 6 and 3 s tapers for the low- and high-frequency bands, respectively. The expected time is calculated as the sum of the event origin time, the asymptotic ray theory traveltime (using *taup*) in the one-dimensional Earth velocity model ak135 from the hypocentre to a point located along the ray path at 61 km depth below sea level at the station, the frequency-dependent traveltime from 61 km depth up to the location of the station, and the ellipticity correction. The traveltime in ak135 is calculated as in point 1, and ellipticity corrections are computed with the algorithm of Euler (2014) after Kennett & Gudmundson (1996).

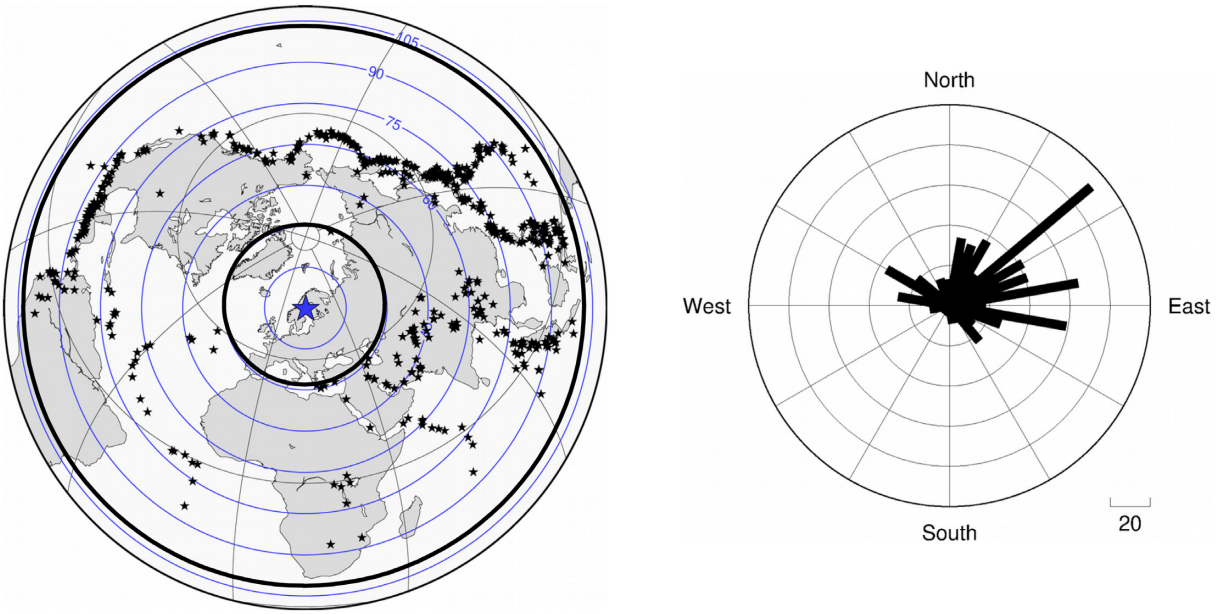

Figure 2. Distribution of teleseismic earthquakes for *P*-waves used for the tomographic inversion for epicentral distances between 30° and 100° (black inner and outer circles). Left-hand panel: Distribution of earthquakes in map view. Right-hand panel: Number of earthquakes per 10°-wide azimuth intervals.

We calculate the frequency-dependent traveltime from 61 km depth to each station based on the EUNAseis model (Artemieva & Thybo 2013). The reference depth of 61 km below sea level is chosen as the deepest Moho in our study region at the SUF station. Low velocities at some stations, caused by interpolation of the EUNAseis model, are corrected to upper crustal values where sedimentary layers are absent. The reflectivity algorithm of Levin & Park (1997) is used to synthesize the propagation of *P* waves from 61 km depth to the station. Starting with an incident pulse as a Dirac function in the mantle, it models the resulting waveform at the station considering all reverberations and conversions in the crustal layers. The waveform is then filtered in the same frequency bands as the data, and the propagation time for each frequency band is chosen at the time of the maximum of the trace. Kolstrup & Maupin (2015) describe the procedure in more detail and discuss the difference between crustal corrections with this method and ray theory.

The expected arrival times obtained with this procedure are used to select the appropriate time windows for further analysis at each station. The windows are pre-aligned using all known sources of time-shifts between stations (different epicentral distance, ellipticity and crustal structure). As the effect of crustal structure and topography is included in this reference time, no crustal correction is necessary at a later stage.

(4) Following the procedure in Kolstrup & Maupin (2015), we apply the Iterative Cross Correlation and Stack (ICCS) algorithm of Lou *et al.* (2013) to obtain a first estimate of the traveltime residuals. The core of this iterative method consists of measuring the time-shifts that ideally align traces with a stack of the traces for this particular event at all stations. It also includes a robust algorithm that rejects traces that have a low cross correlation coefficient and low mean spectral coherence with respect to the stack, enabling an automatic selection of high-quality waveforms. The measured shifts provide relative traveltime residuals with respect to the stack and we do not pick the absolute arrival time of the stack. The absolute arrival time could potentially give information about a possible delay common to all stations due to errors in source parameters or propagation in the lower mantle, but it is not the purpose of this study to analyse this.

(5) As recommended by Lou *et al.* (2013), we finally apply the Multi-Channel Cross Correlation (MCCC) method (VanDecar & Crosson 1990) to the ICCS aligned traces to obtain a refined measurement of the residuals and, importantly, their uncertainties (σ_i).

Due to the relatively monochromatic nature of the signals, there is a higher risk of cycle skipping when picking traveltime residuals on signals filtered for finite-frequency tomography than for ray-based tomography. However, the risk is smallest at low frequencies, where expected delays are much smaller than the dominant period. Therefore, to minimize the risk, we first measure the residuals at low-frequency and provided this residual is below a given threshold, we use it as an *a priori* time lag for the high-frequency band.

We did not correct for the effect of the dispersion related to attenuation, which leads to slightly later arrival times for low than high-frequency waves. In the present geometry of finite-frequency relative tomography, where residuals are demeaned in each individual frequency range separately, the largest effect of this dispersion is related to the long lower-mantle paths for stations at the largest epicentral distances. As the maximum traveltime difference across the full length of the network is 80 s, this effect may cause a maximum delay of up to 0.08 s at the farthest stations compared to the closest stations for the low-frequency interval. This is close to the minimum uncertainty we have assigned to the data. In addition, the effect of the dispersion cancels for events with opposite backazimuths. We consider that this effect on the north–south large-scale variation of our model is well below the uncertainty.

3.3 Finite-frequency body-wave tomography

We determine the relative velocity structure of the upper mantle by applying the finite-frequency tomography method by Hung *et al.* (2004, 2011) to the 74 057 residuals resulting from the previous step. Our dense station coverage at nominally 50 km with long-term data acquisition (2–4 yr at each station) makes it possible to

determine a high resolution *P*-wave velocity model based on body-wave arrivals.

We use multiscale parametrization in terms of wavelet basis functions in 3-D, where the calculations assume an isotropic Earth. The sensitivity kernels G are constructed by the finite-frequency seismic theory (Dahlen *et al.* 2000). The mesh cube is built by using 129 ($2^7 + 1$) x 65 ($2^6 + 1$) x 33 ($2^5 + 1$) = 276 705 nodes with a horizontal grid spacing of 0.174° (corresponding to about 19 km at the surface) and a vertical grid spacing of 25 km between 50 and 800 km depth. We apply the data-adaptive, multiscale approach by Hung *et al.* (2011) to adjust the parametrization to the actual data coverage of the model, whereby the parts that involve more data are better resolved than parts with fewer data points and peripheral parts of the model. With the data-adaptive multiscale parametrization, minimum normal damping (l_2 norm) acts on the coefficients of the wavelet basis functions both in the horizontal and vertical direction instead of acting uniformly on the entire model. This is equivalent to adapting the damping according to the data coverage, damping less the small-scale features in regions of good coverage and better preserving the amplitude of the large-scale features in less covered regions. This has been shown by Hung *et al.* (2011) and confirmed by Kolstrup *et al.* (2015) to give superior results regarding the trade-off between data misfit and model uncertainty. It opens for the recovery of small-scale patterns in areas of high data coverage that would have been smoothed away by damping and smoothing parameters in conventional grid-based parametrizations (Chiao & Kuo 2001; Hung *et al.* 2011). This procedure may also lead to models with sharp heterogeneities that may seem underdamped compared to more traditional models.

The diagonal of the $G^{\mathrm{T}}G$ matrix is used as a proxy for the resolution matrix. The diagonal elements are the squared sum of the sensitivity kernels contributing to the model at the grid nodes, which we present by normalized values (Fig. 3). We restrict the presentation of results to those parts of the models where the resolution matrix values are above a threshold of 0.5 per cent, a value found adequate in previous similar studies (Hung *et al.* 2011; Kolstrup *et al.* 2015). We restrict our model to depths smaller than 800 km after having checked that this choice does not influence significantly the upper part of the model, where the strongest heterogeneities are located.

The area with resolution above the 0.5 per cent threshold increases with depth due to non-vertical incidence of the teleseismic arrivals. The lateral extent of this zone is larger than expected from ray theory due to the width of the finite-frequency kernels, which is about 150 km in diameter at 50 km depth in our long-period range. This leads to resolution outside the region strictly covered by the stations, as resolution tests clearly demonstrate.

The residuals are weighted according to the inverse of their uncertainty, but we adjust all uncertainties to a minimum value of 0.05 s in order to avoid giving an exaggerated weight to some residuals that MCCC has associated with very small uncertainty. In addition, we test the influence of adding station and event terms in the inversions, with different weights as given in Table 1. The event terms remain very small, as expected when using relative residuals where the influence of the source parameters is removed by construction. The amplitude of the station term varies more with the weighting but in no case does it significantly influence the model, showing that we do not propagate in the model significant contributions from imperfect crustal corrections.

We test for optimum damping values by comparing data misfit with model variance (Fig. 4). Following general practice, we choose the damping values where the curvature on the trade-off curves is

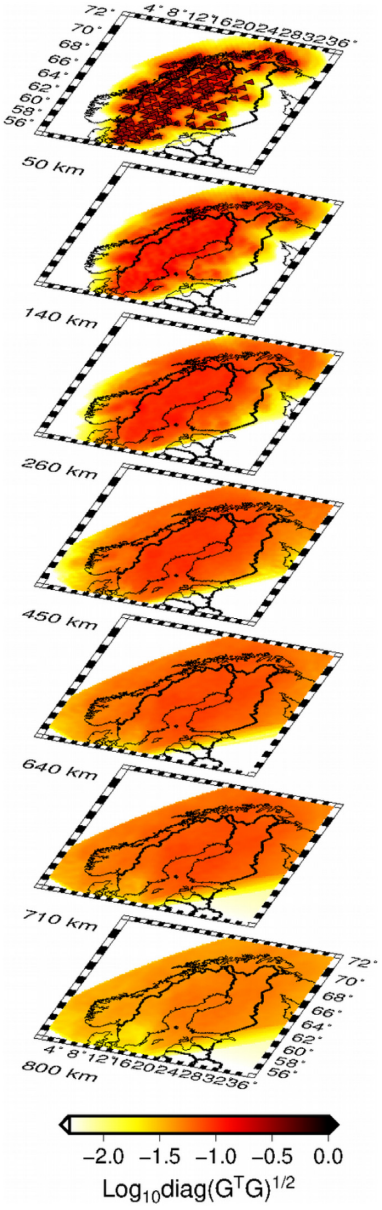

Figure 3. Normalized square-root values of the diagonal of the $G^{\mathrm{T}}G$ matrix as a proxy for the resolution of the velocity models. The minimum logarithmic value of −2.3 corresponds to the chosen resolution threshold of 0.5 per cent.

maximum, corresponding to a data misfit reduction of about 52 per cent. This is rather low, but considering the extent of the study region the assumption of absence of lateral heterogeneity below the maximum depth of the model may not be satisfied and introduce noise in the data.

In addition, unaccounted anisotropy may contribute to lower the variance reduction. Eken *et al.* (2012) have analysed the possible influence of unaccounted anisotropy on *P*-wave tomography in part of the region of our model, using data from the permanent Swedish network. They show that the contribution to the observed residuals by anisotropy can be of the order of ± 0.5 s, which is not negligible. They compare tomographic models with and without correcting the residuals for possible anisotropy-related contributions, using two different methods to evaluate the corrections. The data variance reduction increases to 79 per cent with one of the corrections, from

Table 1. The model parameters tested in the inversion procedure and resolution tests.

Model Parameters	Inversion				Resolution tests		
Number of grid points	65 × 65 × 33 = 139 425		129 × 65 × 33 = 276 705		129 × 65 × 33 = 276 705		
Board size (km^3) (1) Chequers (2) Blocks (3) Cylinders	N\A				(1) dx, dy, dz: 50 to 300 km tested with 11 various models (2) dx, dy, dz: 50 to 300 km tested with 10 various models (3) radius: 50 to 100 km; height: 100 to 200 km tested with 8 various models		
Depth range (km)	50–600	50–670	50–800	50–1000	50–600	50–670	50–800
Noise level added (s)	N\A				0.02 & 0.05		
Damping factors (unitless)	1000, 5000, 8000, 10000, 12000, 15000, 20000				10000		
Weighting (unitless) (event and station corrections)	1–1 & 45–45 & 100–100 & 200–200				1–1		

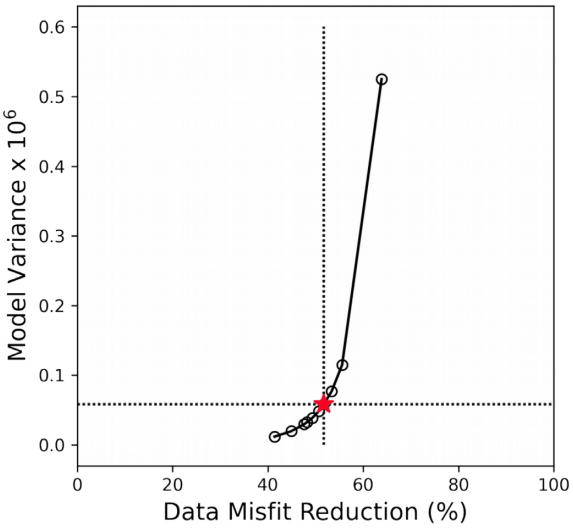

Figure 4. Model variance versus data misfit reduction for various damping values. We choose the optimum damping value at the location of the star symbol.

a value of 51 per cent before correction, very similar to the one in the present study. They also show that large-scale features of tomographic models calculated with and without anisotropy correction are similar, but that the amplitude of the velocity perturbations decreases below ∼200 km depth with anisotropy correction.

In general, large-scale lithospheric anisotropy produces backazimuth-dependent residual patterns which look similar at neighboring stations (Eken *et al.* 2010), and therefore strongly trade-off with heterogeneity at the scale of the interstation distance (about 50 km in this study), but not at much larger scale. Small-scale anisotropy on the other hand is very difficult to deal with in *P*-wave tomography.

The inversion results in a model of the upper mantle *P*-wave velocity structure for most of Fennoscandia for the depth range of 50–800 km. We tested a series of model parameters, such as grid size, model size, depth range, damping, weighting (station and event corrections) and noise levels in the inversion and resolution tests (Table 1). We paid particular attention to the source distribution effects, where uneven azimuthal coverage potentially could cause significant smearing (Fig. 2).

In regional body-wave tomography based on relative traveltimes, two of the most important limitations for studying the structure of the lithosphere and upper mantle are the lack of information on absolute velocities and the lack of resolution of the shallow structure beneath the array because incidence angles are large at shallow level. Limited and uneven distribution of earthquakes on the globe causes another limitation. However, there is no uncertainty related to inaccurate source location and origin time.

4 RESULTS AND RESOLUTION

4.1 Tomographic velocity model

The tomographic model shows relative *P*-wave velocities in the upper mantle across Fennoscandia. The velocities are with respect to the average velocity structure in the study region; it is not with respect to a global average or e.g. ak135. Due to their nature, our measurements do not provide any constraint on this regional average. However, we can use global larger-scale studies to evaluate the regional average in order to interpret our results (Bastow 2012). According to the recent global model by Simmons *et al.* (2021), and in agreement with the seismic velocities expected in cratonic regions, our study region is characterized by higher than global average *P*-wave velocities, in particular in the upper part of the upper mantle. At 115 km depth, the model of Simmons *et al.* (2021) yields in our region *P*-wave velocities about 4 per cent higher than the global average, which means that our −4 per cent anomalies correspond to material with the global average velocity at that depth and that our 0 per cent anomaly corresponds to a velocity 4 per cent higher than the global average. At larger depths, the difference between regional average and global average is smaller, with basically no difference at 275 km depth and less than 1 per cent at 410 km depth.

The resulting *P*-wave velocity perturbations range from −6 per cent to +5 per cent, although illustrated within the range of ± 4 per cent in the figures. The region is characterized by substantial changes between high and low velocities (from >+3 to <−3 per cent) over distances as small as 200 km down to 200 km depth and up to ± 1.5 per cent further down. The velocity anomalies are generally strongest in the shallow part of the model down to ca. 200 km (Figs 5–7). Extremely low-velocity anomalies characterize the lithospheric mantle in the western part below the Caledonian nappes and the offshore sedimentary basins in the northwest and southwest; intermediate positive and negative velocities in the northeastern part; and exceptionally high-velocity anomalies in the central to southeastern part, mainly in the central and southern Svecofennian domains. The velocity anomalies are generally weaker below 200–300 km depth than above, and it appears that the polarity of the anomalies to some degree is reversed across 300 km depth, in particular beneath the Caledonian affected parts of the region. The anomalies are generally weak below 400 km depth.

The Scandes mountain range is generally coincident with the Caledonian areas and is characterized by negative velocity anomalies down to 200 km depth, which may provide evidence for the

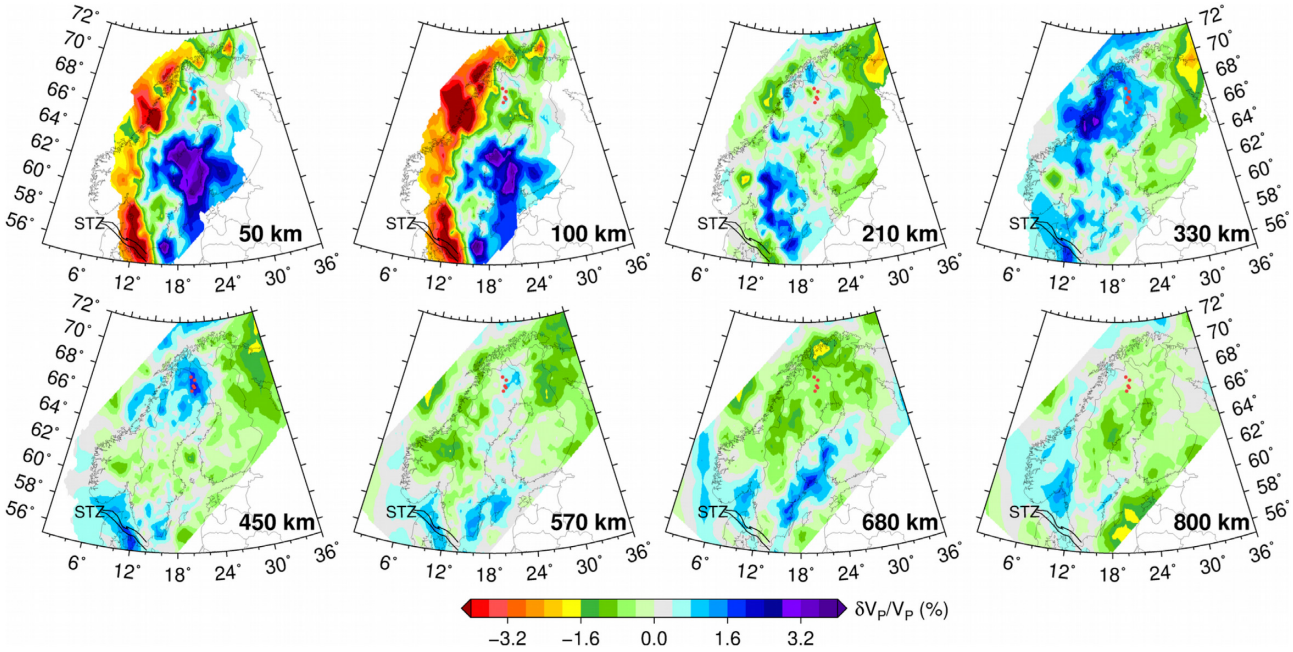

Figure 5. *P*-wave velocity model in map view at selected depths between 50 and 800 km. Red dots illustrate the iron mining districts in the Norrbotten Craton. Annotated depth values on each map refer to any depth point within a 25 km depth range around each stated depth. Only velocity anomalies in the parts of the study area with fair coverage are shown. STZ: Sorgenfrei-Tornquist zone. The whole model with thirty-two depth slices is illustrated in Fig. S1.

cause of the enigmatic high topography. However, the negative velocity anomalies extend into the offshore parts of the region with negative topography, and the lowest velocities down to 200 km occur below the central Scandes and neighboring offshore parts where the topography is shallowest in the Scandes. Profiles A, E, and F in Fig. 6 show that the low-velocity anomalies do not extend deeper than around 200 km below the Scandes and the Caledonian and Sveconorwegian parts. Throughout the model, the strong low-velocity anomalies are underlain by high-velocity anomalies that extend to the transition zone. The model includes a small negative anomaly below 200 km depth that could be related to the Oslo Graben, which rifted in the late Palaeozoic, but the station coverage is sparse here, except for the area around the NORSAR array.

The Transscandinavian Igneous Belt (TIB) in the southern model area appears generally characterized by moderate high-velocity anomalies in the shallow mantle, but its middle part has moderate negative anomalies (Fig. 7). A deep-reaching high-velocity anomaly below southern TIB extends to depths of 800 km (Fig. 6, profile D), and the transition between TIB and the Sveconorwegian domain is abrupt and vertical (Fig. 6, red dashed lines in profiles C and D). A high-velocity anomaly dips southwestward beneath TIB in profile C and correlates with a northwestward dipping feature in profile E (C- junction) that emphasizes the westward dip of the high-velocity core Fennoscandian body beneath the Caledonides. The southernmost part of the model also includes two extreme anomalies of opposite signs down to 300 km depth on either side of the Sorgenfrei-Tornquist Zone.

The Archaean areas in the far north have low velocity in the Lapland Granulite Belt and neutral velocity in Kola-Karelia (Fig. 7). The relatively strong low-velocity anomalies in the deeper Archaean mantle generally extend to a significant depth of 700 km. In the reworked Archaean domain, the velocity anomalies are generally neutral, except for a distinct zone with high velocity in northern Sweden around the iron mining districts in the Norrbotten Craton (marked with red dots in Fig. 5).

The model shows correlation between shallow-velocity anomalies and geological formations (Figs 7 and S2). The southern and central parts of the Svecofennian province are characterized by exceptionally strong high-velocity anomalies that extend down to ca. 200–300 km depth, whereas moderate high-velocity anomalies characterize the northern part of the Svecofennian province. In the Southern domain, the Bergslagen terrane is characterized by near-zero anomalies similar to the reworked Archaean in the north. At depth, the high-velocity anomalies of the Svecofennian domain appear to extend below the Caledonian, and Sveconorwegian affected parts of the shield. The strong negative anomalies below the Caledonides are strongest in the central and northern Svecofennian domains. In contrast, the southern parts of the Norwegian Caledonides, which may be underlain by the southern Svecofennian domain, show smaller negative anomalies although they correspond with the highest topography in Fennoscandia.

4.2 Resolution tests

The vertical and horizontal resolution of the model depends on several factors, including noise level and general quality of data, density of observations, distance and backazimuthal distribution of sources, damping applied and model parametrization (Foulger *et al.* 2013). We use checkerboard and model-driven (block and cylindrical models) tests to assess the lateral and vertical smearing of the model induced by the imperfect resolution power of our data. We show the results using checkers with smooth transitions in the main text and show similar models with sharp transitions in the appendix for comparison. The frequency-dependent theoretical travel residuals are computed by spatial integration of the product of the synthetic model with each of the finite-frequency kernels. In addition to this standard procedure, we demean each set of residuals corresponding to a given event. This is important in order to emulate the zero average of the residuals for each event in the real

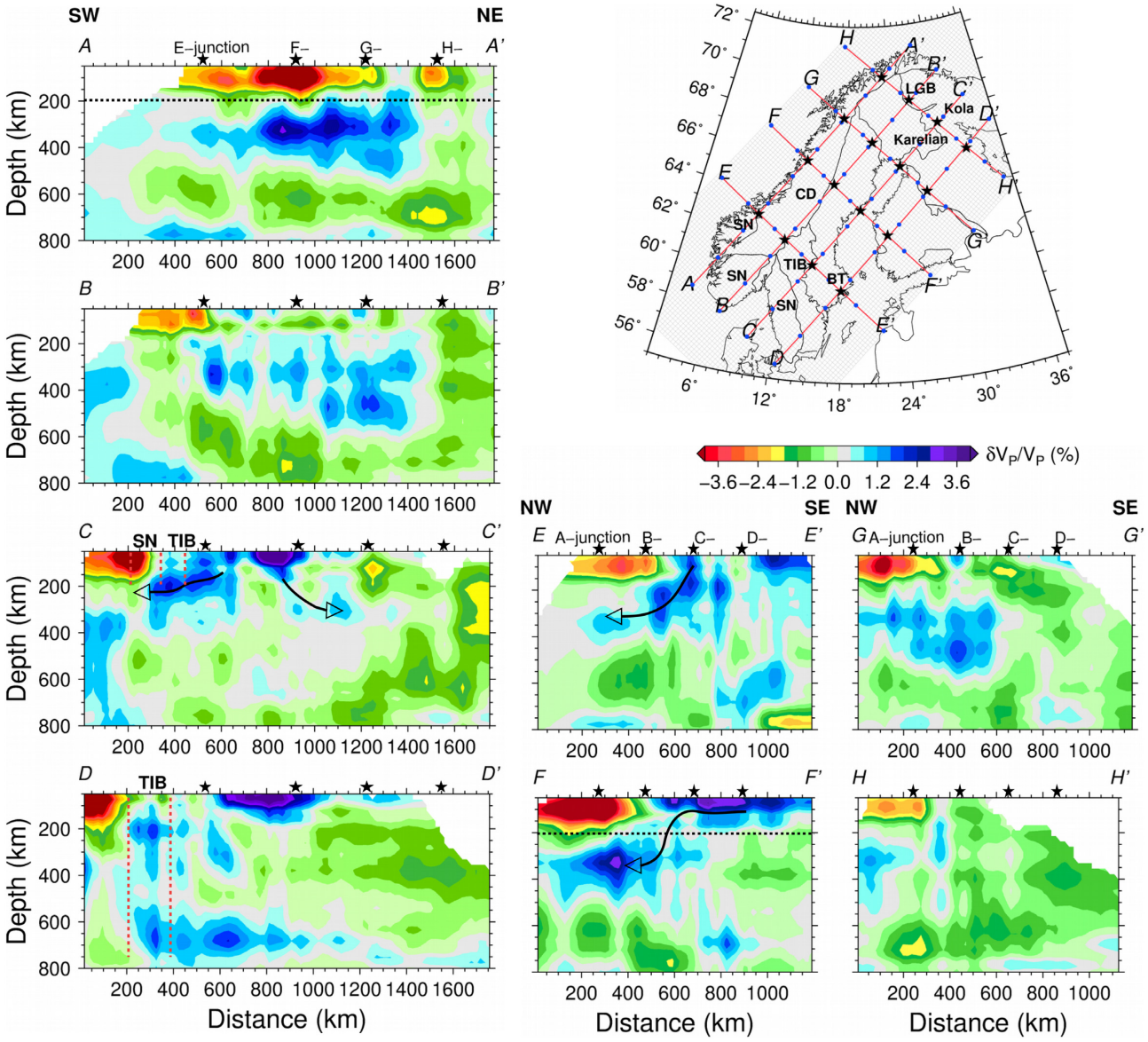

Figure 6. Eight cross-sections illustrating the variation in velocity anomalies across the study region, located in the map with geological formations. The interval between blue dots on the red profile lines is 200 km. Black stars show cross points between profiles. Horizontal black dashed lines on cross-sections A and F indicate strong contrast at 200 km depth. Vertical red dashed lines on cross-sections C and D show the spatial extension of the Transscandinavian Igneous Belt (TIB) and Sveconorwegian (SN) formation on the surface. Only velocity anomalies in the parts of the study area with fair coverage are shown. Grey mesh grids represent the nodes in the inversion. BT: Bergslagen terrane. CD: Caledonian cover. LGB: Lapland Granulite Belt.

data processing procedure. We add 0.05 sec white noise to the theoretical traveltime residuals before inversion. All resolution tests are based on the same source/receiver geometry, frequency bands and inversion parameters as for the observed data.

All body-wave tomography methods will lead to anomaly smearing, which is most significant in the vertical direction due to the steep incidence of signals from distant earthquakes. We observe that NNE-directed profiles show strong smearing, potentially related to the dominant number of events in the region around Japan. However, reducing the number of traveltime picks from this direction does not significantly reduce the smearing. Structures appear better resolved horizontally than vertically, which is expected due to the steep incidence angles for teleseismic waves and the location of Scandinavia with respect to the world seismicity.

Tests with a series of checkerboard sizes indicate a vertical and horizontal resolution limit of around 150 km. Fine checker sizes ($150 \times 150 \times 150$ km^3) demonstrate good vertical and horizontal resolution in the first checker layer (down to ca. 200 km depth). At larger depth, some layers (Fig. 8) seem to be biased towards low (284 km depth) or high (425 km depth) velocities. This is likely related to a sort of aliasing phenomenon between the small-scale of the present checkerboard and the multiscale parametrization that favours large-scale features if resolved by the data. Note that this bias is smaller in the checkerboard with large cells and absent from the model-based tests in Fig. 12, and we do not expect the real model to suffer from such aliasing effect. Resolution deteriorates gradually below 550 km and is almost lost below 700 km depth (Figs 8 and 9). Coarse checker sizes (e.g. $300 \times 300 \times 200$ km^3) are better resolved throughout the model (Figs 10 and 11), and the

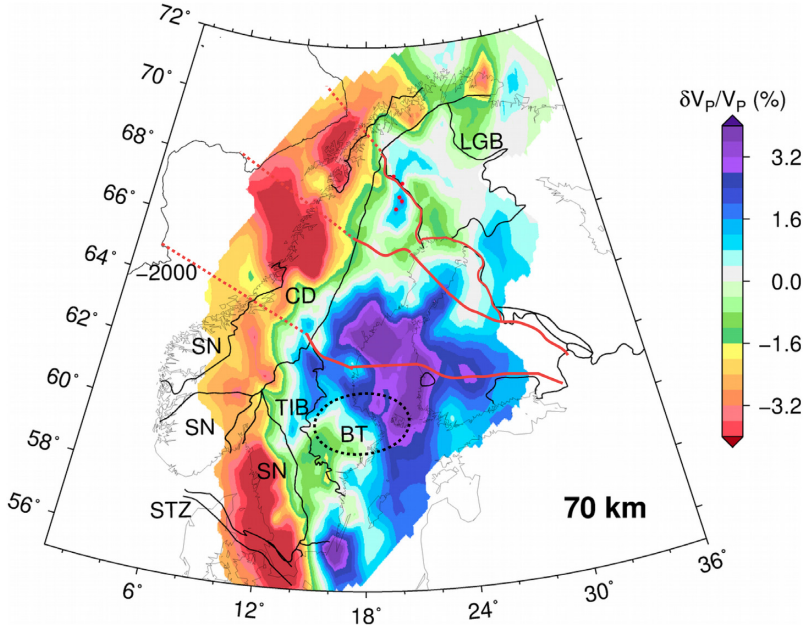

Figure 7. The tomography model at depth 70 km with superimposed geological formations (solid black lines). Red solid lines divide the Svecofennian province into three domains; dashed lines show possible domain extension beneath the Caledonides. Red dots illustrate the iron mining districts in the Norrbotten Craton. The −2000 m bathymetry contour with a thin solid line roughly represents the outer margin of the Vøring Plateau. Dashed ellipse illustrates the Bergslagen terrane (BT). STZ: Sorgenfrei-Tornquist Zone. TIB: Transscandinavian Igneous Belt. CD: Caledonian cover. SN: Sveconorwegian. LGB: Lapland Granulite Belt. More overlay maps are shown in Fig. S2.

checker shapes are almost fully recovered throughout the whole model down to a depth of 800 km, with an apparent reduction in resolution in part of the transition zone. All depth levels of the checkerboard tests are illustrated in Figs S3 and S4.

We further investigate the resolution limits with synthetic block and cylindrical models. As a brief example, the results for five separate cylindrical synthetic anomalies representing possible geological structures in the model are illustrated in Fig. 12. All anomalies have 75 km radii. Depth ranges are 61–261 km for the models in southern Lofoten and southern Sweden; 200–400 km for the central Baltic Shield; 50–200 km for central Sweden. The cylindrical synthetic anomalies are defined as: (1) Low-velocity (−4 per cent) and (2) high-velocity (+4 per cent) anomalies couplets representing the dipole-like structure in southernmost Sweden, which might be related to the Sorgenfrei-Tornquist Zone (Thybo 2001). (3) A low-velocity anomaly (−4 per cent) to the south of Lofoten is chosen to detect any possible leakage (especially horizontal smearing) from the offshore zone into coastal central Norway. (4) A shallow high-velocity anomaly (+4 per cent) in the central Svecofennian domain to test the extent of the strongest anomaly in the results. (5) A deep low-velocity anomaly (−4 per cent) in the central Baltic Sea to test the accuracy of the low velocities beneath the dominant high velocities in the region. We interpret from the recovered anomalies (1) and (2) that the southern edge of the region is well resolved, including the Sorgenfrei-Tornquist Zone as well as possible mantle structures related to the Trans-European Suture Zone (TESZ). High-velocity anomaly (2) has better resolution than low-velocity anomaly (1) regarding horizontal and vertical smearing. For anomaly (3), there is minimal horizontal leakage while there is some vertical smearing. Anomaly (4) in central Sweden is well resolved in the region with very strong high-velocity anomalies. The deep low-velocity anomaly (5) beneath the core of the strong high-velocity anomaly is also well recovered horizontally, leading to some vertical leakage, particularly to deeper levels.

5 DISCUSSION

We present a new model of seismic *P*-wave velocity anomalies for most of Fennoscandia based on finite-frequency tomography. Earlier high resolution tomographic studies have covered part of the region (Husebye *et al.* 1986; Bannister *et al.* 1991; Shomali *et al.* 2002; Sandoval *et al.* 2004; Eken *et al.* 2007; Medhus *et al.* 2012; Kolstrup *et al.* 2015) or have been part of regional European or global models with lower resolution than presented here (Zhu *et al.* 2015). Our model shows strong amplitudes of up to 6 per cent, lateral velocity contrasts of up to ± 3 per cent over horizontal distances of around 200 km down to 200 km depth, and amplitudes up to ± 1.5 per cent further down. These amplitudes are considered to be very large for a cratonic region and are significantly larger than what has usually been inferred in this region (e.g. Eken *et al.* 2007). Our large amplitudes may partly be attributed to the refined damping procedure based on wavelet parametrization of the model. Hung *et al.* (2011) introduced this procedure in their tomography of Tibet and demonstrate that, other things being equal, more than twice larger velocity variations are inferred with the present damping procedure than with traditional norm-damping normalization. Kolstrup *et al.* (2015) also used the damping procedure of Hung *et al.* (2011) and infer a variation of ± 2.5 per cent in a partly overlapping region to the southwest of our study area, a contrast similar to the one inferred by Medhus *et al.* (2012) in the same region. We also note the good amplitude recovery in our synthetic resolution tests. All these elements point to the credibility of our velocity variations. We acknowledge that the interpretation in a cratonic setting of such velocity contrasts is challenging, but Kolstrup *et al.* (2015) provide some clues for an interpretation of such contrasts in terms of realistic combination of temperature and compositional variations.

Several studies (e.g. Ebbing & Olesen 2005; Stratford *et al.* 2009; England & Ebbing 2012; Frassetto & Thybo 2013) have indicated that the high topography in the Scandes may be caused by isostatic

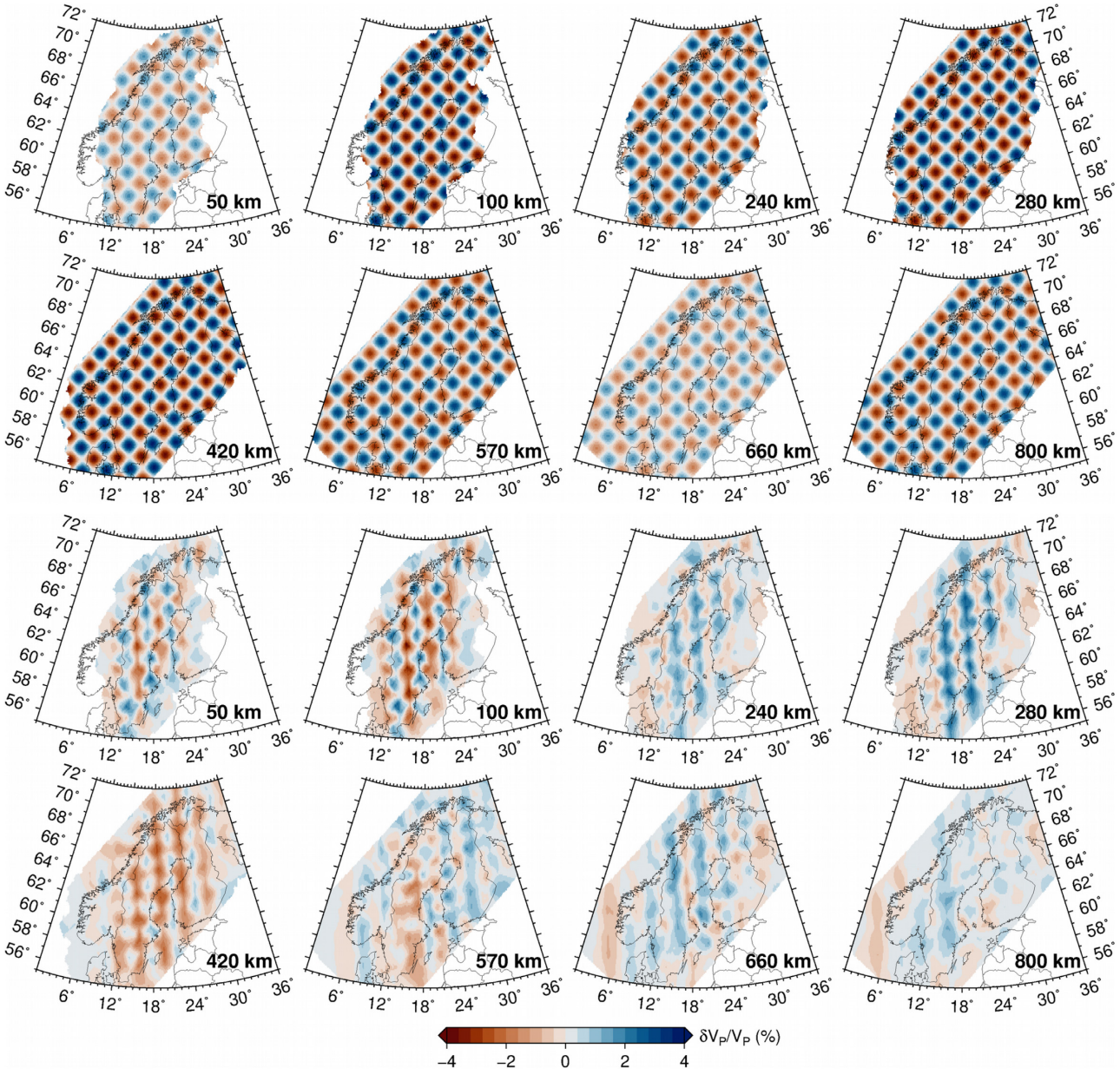

Figure 8. Results of the checkerboard test illustrated by depth slices for board size 150 × 150 × 150 km^3. Top panel: Synthetic input for the test, $\Delta \ln V_P = \pm 4$ per cent. Bottom panel: Inversion result for the synthetic data. More depth levels with sharp-edge checkers are illustrated in Fig. S3.

or dynamic anomalies related to low-velocity anomalies in the lithospheric and sublithospheric mantle. Our results show that the low velocities below the Scandes extend to depths of only around 200 km along the whole coastline to the North Atlantic Ocean with significant variation in anomaly amplitude which does not correlate fully with the variation in topography. The velocity anomaly is moderately negative below the southern Scandes, which forms the highest part of the Scandes mountain range where the resolution, however, may be low due to poor coverage. Moreover, the low-velocity anomaly is underlain by a very large positive velocity anomaly in the northern Scandes and moderate amplitude anomalies in the southern Scandes. If the high topography of the Scandes is related to the low-velocity anomalies, it is puzzling that the strong, shallow low-velocity anomaly down to 200 km depth extends far into the North Atlantic Ocean below the subdued continental shelf and possibly into the oceanic realm where the shelf is narrow. Makushkina *et al.* (2019) show that the 410-discontinuity is not deflected in our study region. Therefore, the low velocities in this area are unlikely to be caused by a thermal anomaly that originates in the lower mantle.

The area with a dominant, shallow high-velocity anomaly in central Sweden and southwestern Finland is located in a zone characterized by low topography (Figs 5, 7 and 13). This combination may isostatically be explained as a combination of cold mantle and thick, high density lower crust (Frassetto & Thybo 2013). However, the mantle in Finland below very thick crust is characterized by neutral to slightly negative velocity anomalies, which may indicate that other mechanisms are affecting the topography within this part of the shield. We test for possible isostatic effects on the topography from the lithospheric mantle by cross plotting relative velocity at various depth levels versus hypsometry in the relevant geological formations (Fig. 13). We find linear relations with a coefficient of determination (R^2) of ca. 50 per cent in the

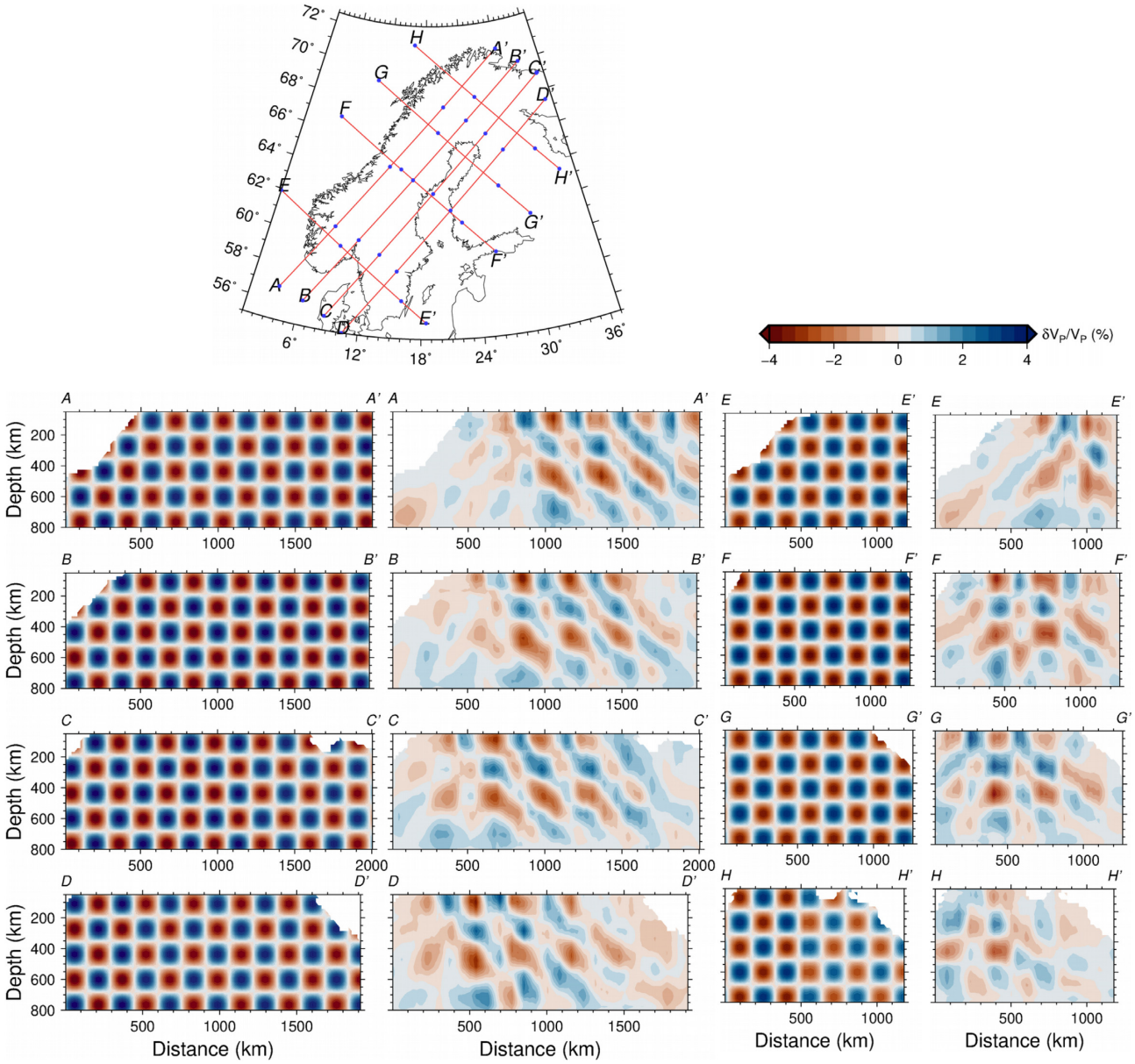

Figure 9. Results of the checkerboard test illustrated along eight profiles for board sizes 150 × 150 × 150 km^3. Top panel: Profiles tested. Bottom panels: Synthetic input with velocity perturbations and inversion result for the synthetic data, $\Delta \ln V_P = \pm 4$ per cent. The interval between blue dots on the red profile lines is 200 km.

central and ca. 60 per cent, for 95 per cent confidence interval, to depths around 100 km in the southern Svecofennian domains, whereas the northern Svecofennian domain does not indicate any correlation. Our test includes both the parts with exposed Svecofennian crust and their inferred continuation below the Scandes in the Caledonian and Sveconorwegian provinces. We do not find similar correlation in other parts of Fennoscandia. Our observation that, if the density variation in the lithosphere correlates with the velocity anomalies, this density variation affects the observed topographic variation. One may speculate if the cause of the density variation is variation in temperature or composition/metamorphic grade of the rocks in the lithospheric mantle or a combination of both.

The preserved evidence of the Caledonian orogeny in the Baltic Shield consists of a series of relatively thin nappe structures in the uppermost crust. Therefore, a correlation between the Caledonides and the deep crustal and mantle lithosphere is not expected. We find the extremely low-velocity anomalies below the Caledonian affected areas surprising, and it is uncertain if they are related to Caledonian structure. We suggest that the low velocities in the upper mantle below the high topography in the northern and southern Scandes indicate that coincident low densities in the uppermost mantle may support the high topography (e.g. Ebbing 2007; Stratford *et al.* 2009; Medhus *et al.* 2012).

The strongest low-velocity anomalies appear in the onshore and offshore parts between the two domes of the Scandes and around southern Lofoten. We observe that the anomalies extend far into the offshore part, mainly in the continental mantle to depths of ca. 200 km. The relation between this continuous low-velocity anomaly below both relatively high onshore topography and subdued offshore shelves is not clear. Low velocities in the continental lithosphere beneath Lofoten and south of Lofoten may be bounded by

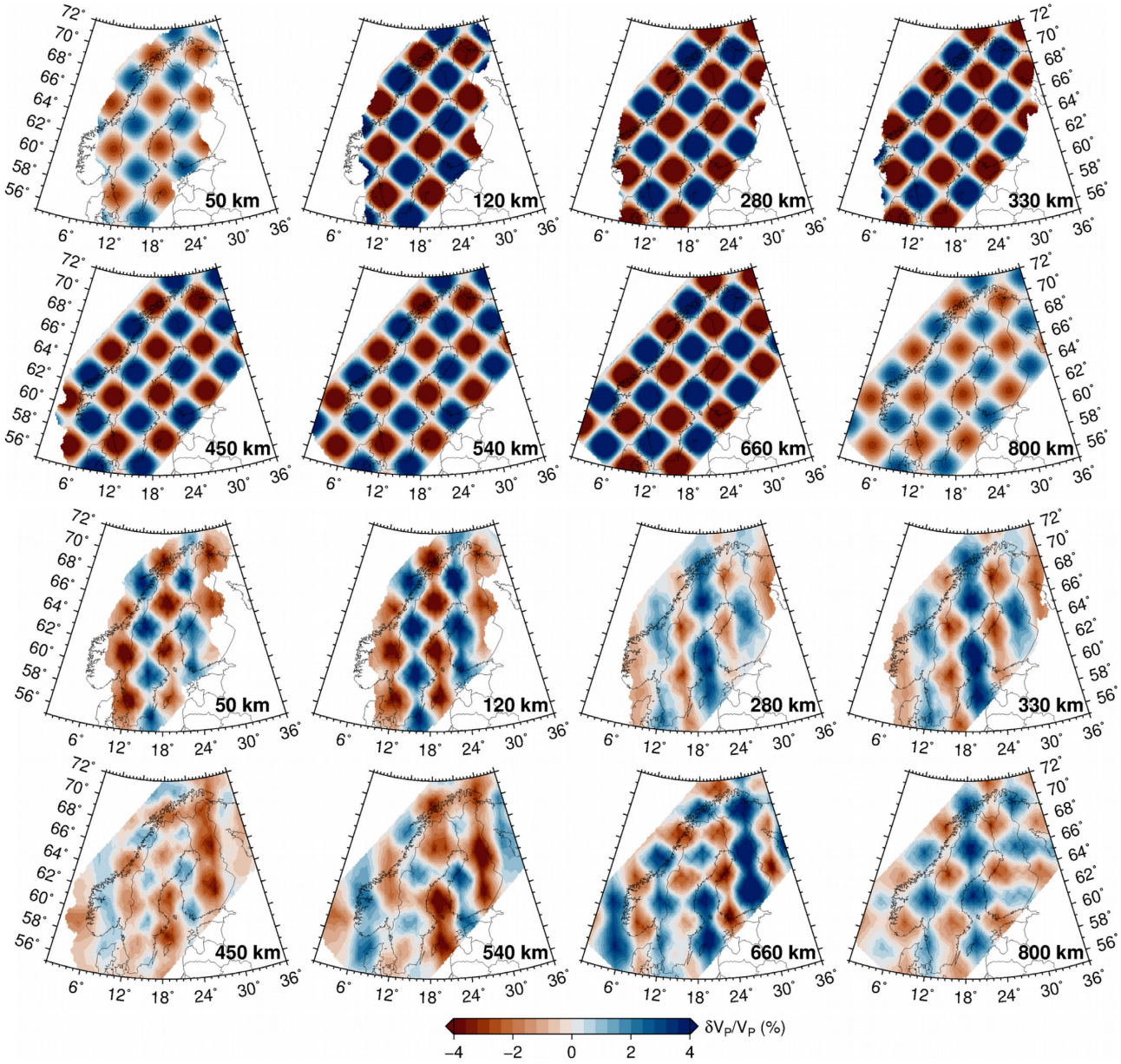

Figure 10. Results of the checkerboard test illustrated by depth slices for board size 300 × 300 × 200 km^3, $\Delta \ln V_P = \pm 4$ per cent. Top panel: Synthetic input for the test. Bottom panel: Inversion result for the synthetic data. More depth levels with sharp-edge checkers are illustrated in Fig. S4.

NW–SE directed geological shear zones in the region at the boundaries between the three main Svecofennian domains (Figs 5 and 7, Supporting Information Figs S1 and S2).

Sharp and strong horizontal and vertical velocity contrasts (Figs 5 and 6) demonstrate significant structural differences between the shallow and deep structures in Norway (Scandes) and between the upper mantle in Norway and Sweden (the young Caledonides and Scandes versus the Baltic Shield proper). In particular, our model supports the hypothesis that the topography of the southern Scandes, with thin crust (30–36 km) and no crustal root (Stratford *et al.* 2009), is instead supported by low density, low-velocity, high temperature material in the uppermost mantle (e.g. Artemieva 2003; Gradmann *et al.* 2013). In contrast, southern Sweden has a thick crust (up to 50–60 km thick) and thick shield lithosphere with high velocities, which is characterized by low temperature (Artemieva 2007).

The arched low-velocity anomalies in southern Scandinavia (along the west coast of Norway into southernmost Sweden and Denmark) is in agreement with other recent results in smaller parts of the region (e.g. Medhus *et al.* 2012; Rickers *et al.* 2013; Kolstrup *et al.* *2015*), although the amplitude of the anomalies is stronger in our model and the location of the smallest velocities generally extends further to the south than earlier interpreted (Figs 5 and 7, Supporting Information Figs S1 and S2). According to Rickers *et al.* (2013), the spreading of a plume or hotspot beneath Iceland into southern Scandinavia may explain the low velocities in this region. The supplementary data of Zhu *et al.* (2015) also show relatively low velocities in southernmost Sweden and southern Lofoten as in our model, although with lower amplitude. Zhu *et al.* (2015) interpret high attenuation down to 200 km in southern Norway and low attenuation in southern Sweden outside the Caledonian region which coincide with our strong positive velocity anomaly.

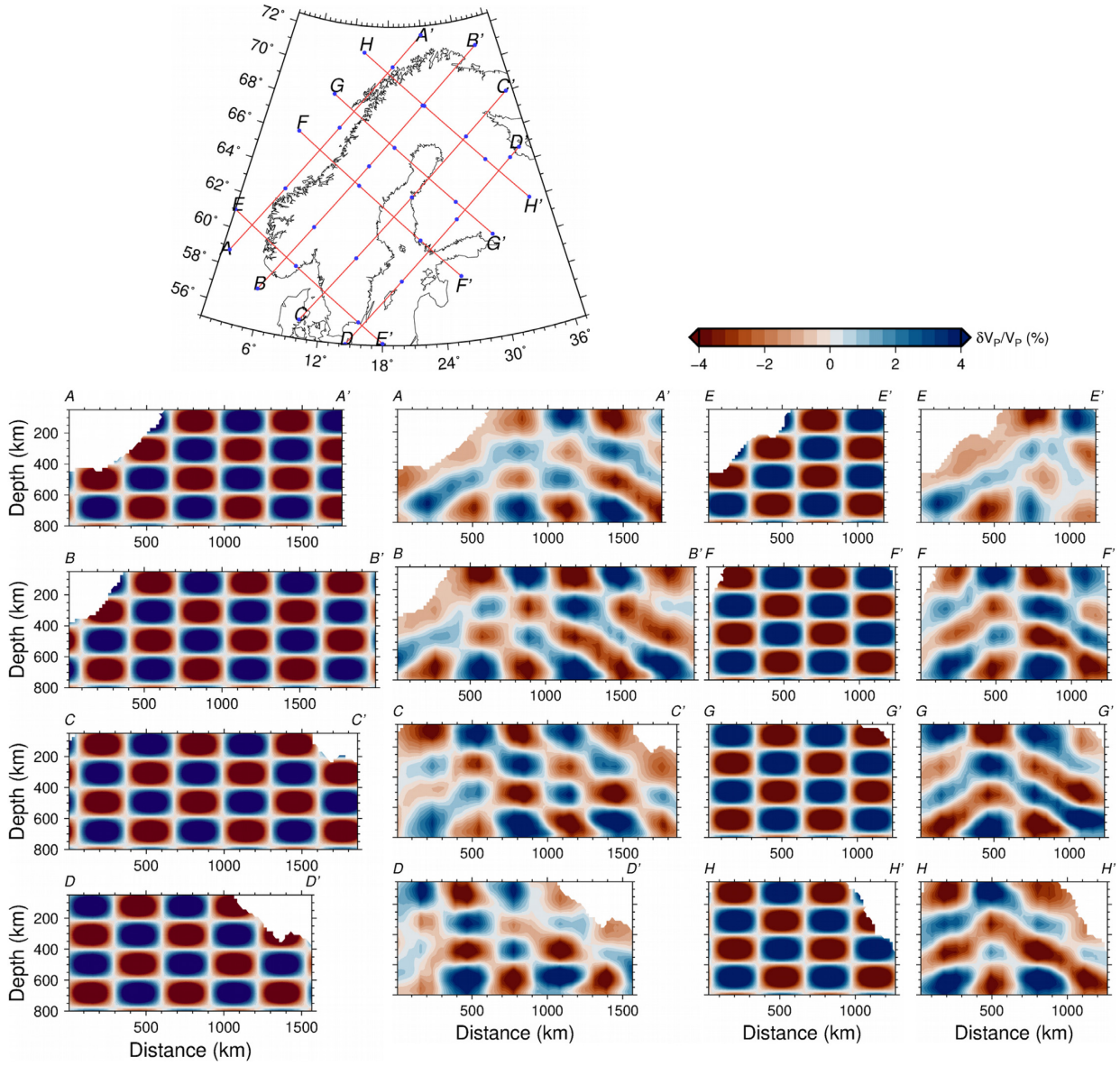

Figure 11. Results of the checkerboard test illustrated along eight profiles for board sizes 300 × 300 × 200 km^3. Top panel: Profiles tested. Bottom panels: Synthetic input with velocity perturbations and inversion result for the synthetic data, $\Delta \ln V_P = \pm 4$ per cent. The interval between blue dots on the red profile lines is 200 km.

Throughout most of the region, the low-velocity anomaly below the Caledonian and Sveconorwegian parts is underlain by relatively strong high-velocity anomalies that may indicate the presence of well-preserved Svecofennian lithosphere below the Caledonides and Sveconorwegian regions, as well as the reworked Archaean domain in the north. Thus, we interpret these high velocities below the strong negative anomalies as evidence that the original Svecofennian and Archaean mantle is preserved throughout Fennoscandia, with the strongest positive velocity anomalies in the central parts of the southern and central Svecofennian domains, and deeper below the Caledonian and Sveconorwegian provinces.

We observe the strongest, shallow high-velocity anomalies in central Sweden and southwestern Finland (Figs 5 and 7). Previous high resolution studies (e.g. Pedersen *et al.* 2013; Silvennoinen *et al.* 2016) have identified very high seismic velocities in the upper mantle of southern Finland to 200 km depth and an indication of a 300 km thick lithosphere (Sandoval *et al.* 2004). Our results show relative velocities at each depth interval. In addition, we identify exceptionally high-velocity anomalies in central Fennoscandia, which are 3 per cent higher than in central and northern Finland, where other authors identify high absolute cratonic velocity by using surface wave study (Silvennoinen *et al.* 2016). Therefore, our observation indicates that the upper mantle to ca. 200 km depth in the southern and central Svecofennian domains has unusually high absolute velocity compared to other cratons. We suggest that the core of the present craton is located in the central area with the strongest high-velocity anomaly, even though the craton was built by northward collision of terranes onto the Archaean terranes in the far north. Our observations indicate strong modification of the upper mantle in the Archaean parts and the marginal parts of the Svecofennian craton, whereas the central craton has been protected from severe modification and the exceptionally high-velocity anomalies indicate the presence of pristine cratonic mantle.

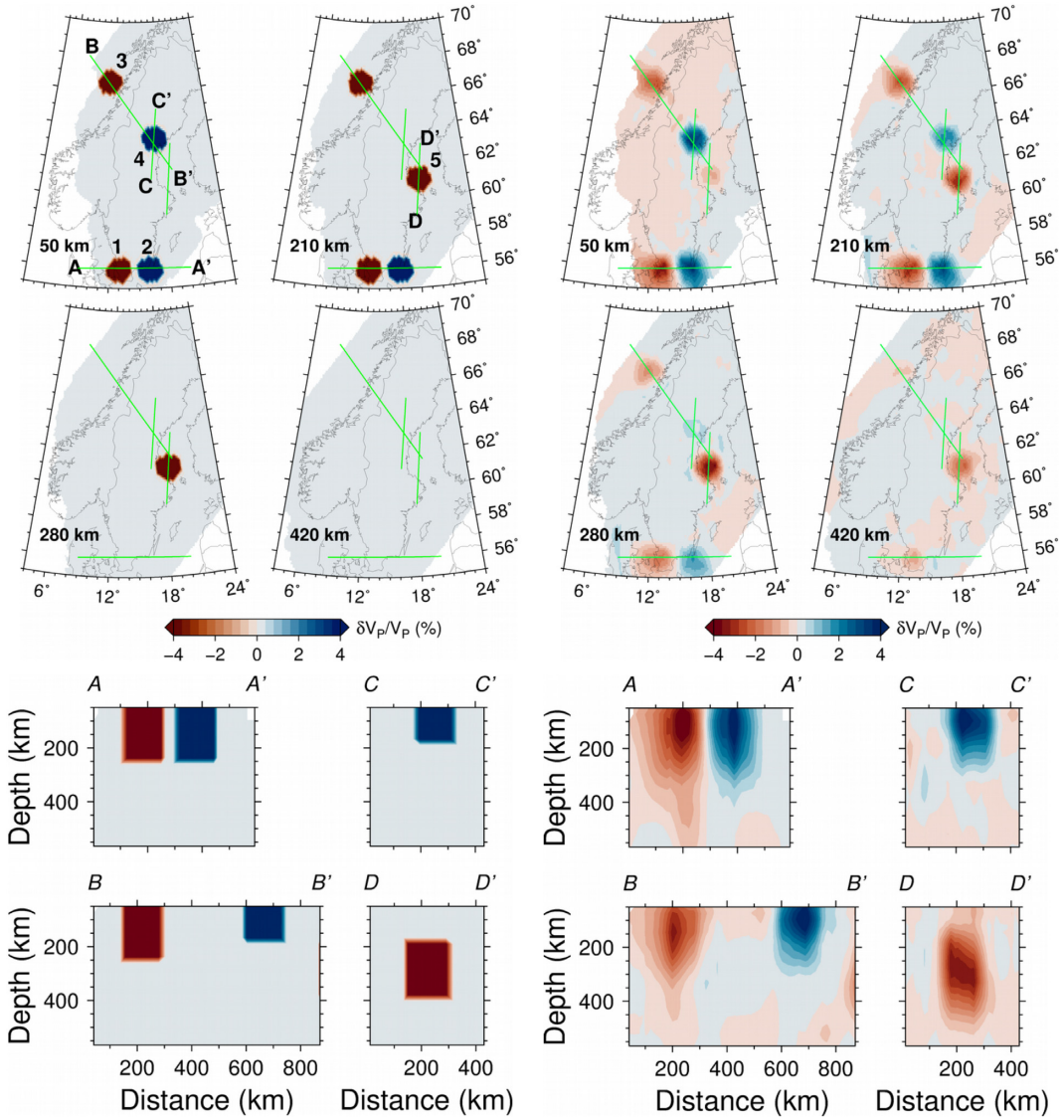

Figure 12. Synthetic test with five separate cylindrical anomalies: Three high-velocity (blue anomalies, +4 per cent) and two low-velocity (red anomalies, −4 per cent) structures observed in the results were tested. All models have 75 km radii. Depth ranges are 61–261 km for the models in southern Lofoten and southern Sweden (1, 2, 3); 50–200 km for central Sweden (4); and 200–400 km for the central Baltic Shield (5).

Strong positive and negative anomalies in southernmost Sweden provide evidence for a deep anomaly contrast across the Sorgenfrei-Tornquist Zone to depths of 250–300 km (profiles C and D in Fig. 6). The resolution test shows that the model is well resolved regarding both lateral and depth extent of the anomalies in this part of the study area. This observation is significant because earlier tomographic models indicate that the cratonic lithosphere has a maximum thickness of 150 km in this southern part of the craton (Shomali *et al.* 2002). The extremely low velocities in the shallow upper mantle in the southernmost part of profiles C and D (Fig. 6) are probably related to the extended and thinned part of the Baltica Plate in the North Sea area around Denmark at the southwestern edge of the craton. Moreover, the details of the high-velocity anomaly in the southwestern and central part of profile C (Fig. 6) could indicate south and northward dipping features from around km 700 horizontal distance in the southern Bothnian Bay, which may be related to hitherto unknown palaeo-subduction in the region.

Previous controlled-source seismic studies of the crust and uppermost mantle in Fennoscandia have shown structures that indicate early subduction and continental collision. BABEL Working Group (1990) observe dipping normal-incidence reflections, supplemented by wide-angle reflections, into the upper mantle which are interpreted as evidence for 1.87 Ga Palaeoproterozoic subduction in the Bothnian Bay around 64°N. Abramovitz *et al.* (1997) present extensive observations of normal-incidence and wide-angle reflections which indicate Palaeoproterozoic subduction in the Baltic Sea around 57°N. The latter authors further observe that the seismic velocity changes abruptly from 8.2 to 7.8 km/s across the upper mantle reflector, which indicates a significant change in uppermost mantle composition. Our results show indications for the continuation of these structures into the upper mantle. For the northern structure, we observe a clear abrupt change in velocity in the uppermost mantle from high velocity in the south to lower velocity in the north (Fig. 14, profiles A, B, marked with black dashed lines) coinciding with the crustal to uppermost mantle structure observed by

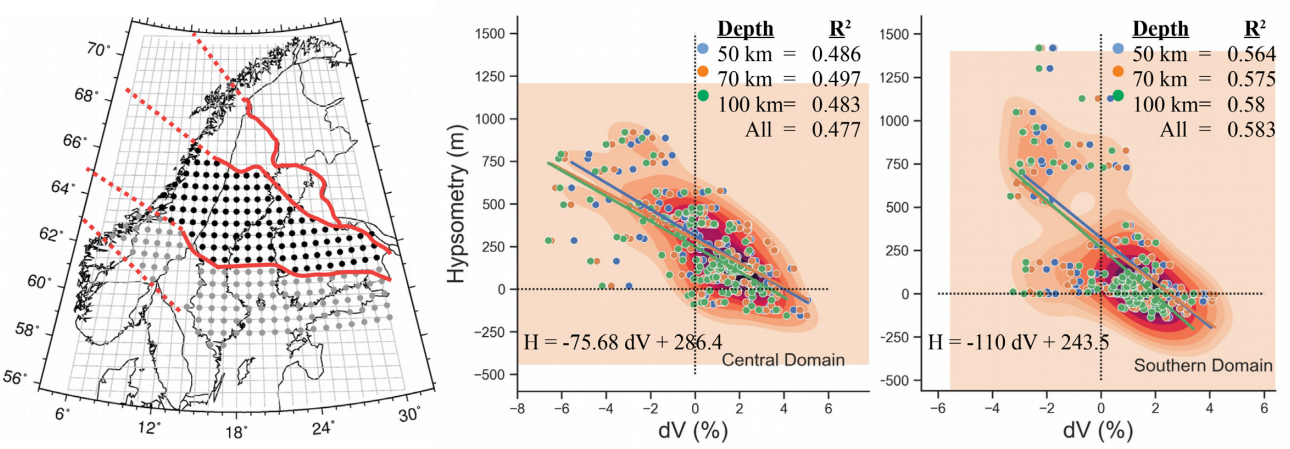

Figure 13. Test of possible isostatic support of the topography by the uppermost lithospheric mantle by cross plots of relative velocity (dV per cent) and hypsometry (m) at three depth levels down to ca. 100 km in the central and southern Svecofennian domains. Left panel: Map showing the considered geological formations. Solid and dashed red lines divide the Svecofennian province into its three domains. Black and grey dots on the map illustrate locations where data points were read, in central and southern domains, respectively. Middle and right panels: Cross plots from the central and southern Svecofennian domains. Red hue contours represent normalized densities of the number of observations. R^2 is in 95 per cent confidence interval. Bisquare weighting, is used to downweight extreme outliers. Coloured lines show best fit lines for the three depth levels, which indicate a correlation between dV (per cent) and hypsometry (m) in the two domains. The best fit line is described for all depth levels for the two cases.

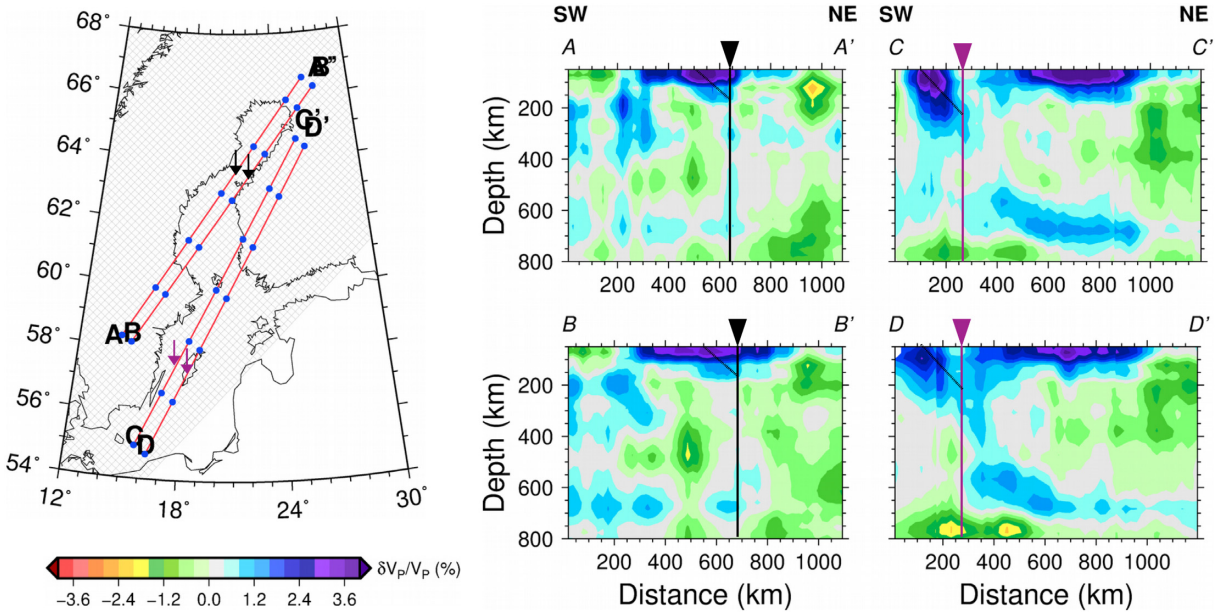

Figure 14. Four cross-sections across published Palaeoproterozoic collision sutures. The black arrows on the map and the cross-sections (A, B) show the location of the proposed subduction-related structure in the uppermost mantle by BABEL Working Group (1990). The purple arrows at the island Gotland and cross-sections (C, D) show the location of the dipping proposed subduction-related structure in the uppermost mantle (Abramovitz *et al.* 1997).

BABEL Working Group (1990). The profiles show a weak continuation of the high velocities steeply dipping into the upper mantle at the crustal/sub-Moho transition. For the southern structure (Fig. 14, profiles C, D, marked with black dashed lines), we observe that very high-velocity anomalies in the south continue as a steeply north-dipping anomaly in the upper mantle to depths of 300–400 km below lower-velocity anomalies in the north, similar to the results down to 80 km depth by Abramovitz *et al.* (1997). We interpret this feature as the image of a Palaeoproterozoic subduction slab which has been preserved for 1.8 Gy in the lithosphere to a depth of at least 250 km. The profiles indicate a continuation of the lithospheric strong positive velocity anomaly into a high-velocity anomaly in the Transition Zone. However, these anomalies may be uncorrelated as the anomaly amplitude is weak in the depth interval of 350–500 km, and the apparent correlation is difficult to explain in a plate tectonic framework. Similar dipping features have been observed by Eken *et al.* (2007) in the upper mantle between latitude 60° and 64° N in a *P*-wave tomography model of the east coast of Sweden. Their anomaly is however situated further northwest than in our study.

6 CONCLUSIONS

We present a new high- resolution model of the variation of seismic *P*-wave velocity in the upper mantle down to 800 km depth

below Fennoscandia based on relative traveltime inversion using finite-frequency sensitivity kernels. We use new data from the ScanArray collaborative project, which has completed the coverage of the whole Fennoscandian shield by broad-band seismological data at a nominal station distance of 50 km.

Our new model allows us to make the following conclusions:

(i) The Fennoscandian upper mantle is characterized by strong velocity contrasts (>6 per cent) over lateral distances as short as 200 km.

(ii) The low velocities in the upper mantle below the high topography support the hypothesis that the northern and southern Scandes are at least partly supported by low-density, low-velocity material in the uppermost mantle above 200 km depth.

(iii) We observe a linear correlation between hypsometry and velocity anomalies to 100 km depth in central Fennoscandia in the region from the Proterozoic lowlands into the Caledonian/Svenorwegian provinces with high topography.

(iv) We observe exceptionally high-velocity anomalies in the central part of Fennoscandia in the central and southern Svecofennian domains. We propose that the pristine upper mantle of the present Fennoscandian cratonic core has been protected from modification whereas the Archaean and marginal Svecofennian parts have experienced significant modification of the upper mantle.

(v) High-velocity anomalies beneath the strong negative anomalies below the Scandes indicate that original Svecofennian and Archaean mantle is preserved throughout Fennoscandia, including the Caledonian and Svenorwegian provinces.

(vi) A strong high-velocity north-dipping anomaly in the southern Baltic Sea coincides with a Palaeoproterozoic subduction/collision structure in the crust and uppermost mantle.

ACKNOWLEDGMENTS

NB acknowledges the hospitality at CEED and DEEP Norwegian Research School during her visits to UiO. All computations have been done on the computers of the University of Oslo and we would like to thank the IT staff for their support. We thank Shu-Huei Hung from the National Taiwan University for sharing the FORTRAN-based code for calculation of finite-frequency body-wave tomography. Figures were prepared using Generic Mapping Tools (Wessel *et al.* 2013). We thank Ian Bastow and Richard England for comments and suggestions that greatly contributed to improve the manuscript.

This work is a part of the PhD study of NB, which is supported by Independent Research Fund Denmark by grant number 4002–00552B to HT. Funding has been provided by TUBITAK grant No. 1199B472000709, National Science Foundation of China grant No. 92055210, and the MOST special funds for GPMR State Key Laboratory (CUG-Wuhan) grant No. GPMR2019010. VM acknowledges support from the Research Council of Norway through its Centers of Excellence funding scheme, Project Number 223272.

DATA AVAILABILITY

The data underlying this paper are available in the European Integrated Data Archive (EIDA) from the GEOFON data centre (International Federation of Digital Seismograph Networks [FDSN] network code 1G 2012–2017, doi: 10.14 470/6T569239); the Norwegian Seismic Array (NORSAR) at https://www.fdsn.org/networks/detail/NO/(Norwegian Seismic Array); and from Helsinki at https://doi.org/10.14470/UR044600 (Institute of Seismology, University of Helsinki, 1980). Data from the Northern Finland network are available at https://www.fdsn.org/networks/detail/FN.

REFERENCES

Abramovitz, T., Berthelsen, A. & Thybo, H., 1997. Proterozoic sutures and terranes in the southeastern Baltic Shield interpreted from BABEL deep seismic data, *Tectonophysics,* **270**(3–4), 259–277.

Andersen, T. & Sundvoll, B., 1995. Neodymium isotope systematics of the mantle beneath the Baltic shield: evidence for depleted mantle evolution since the Archaean, *Lithos,* **35**(3–4), 235–243.

Anell, I., Thybo, H. & Artemieva, I.M., 2009. Cenozoic uplift and subsidence in the North Atlantic region: geological evidence revisited, *Tectonophysics,* **474**(1–2), 78–105.

Anell, I., Thybo, H. & Stratford, W., 2010. Relating Cenozoic North Sea sediments to topography in southern Norway: the interplay between tectonics and climate, *Earth planet. Sci. Lett.,* **300**(1–2), 19–32.

Artemieva, I.M., 2003. Lithospheric structure, composition, and thermal regime of the East European Craton: implications for the subsidence of the Russian platform, *Earth planet. Sci. Lett.,* **213**(3–4), 431–446.

Artemieva, I.M., 2007. Dynamic topography of the East European craton: Shedding light upon lithospheric structure, composition and mantle dynamics., *Glob. Planet Change,* **58,** 411–434.

Artemieva, I.M. & Meissner, R., 2012. Crustal thickness controlled by plate tectonics: a review of crust-mantle interaction processes illustrated by European examples, *Tectonophysics,* **530–531,** 18–49.

Artemieva, I.M. & Thybo, H., 2013. EUNAseis: a seismic model for Moho and crustal structure in Europe, Greenland, and the North Atlantic region, *Tectonophysics,* **609,** 97–153.

BABEL Working Group, 1990. Evidence for early Proterozoic plate tectonics from seismic reflection profiles in the Baltic Shield, *Nature,* **348,** 34–38.

Bannister, S., Ruud, B.O. & Husebye, E., 1991. Tomographic estimates of sub-Moho seismic velocities in Fennoscandia and structural implications, *Tectonophysics,* **189,** 37–53.

Bastow, I.D., 2012. Relative arrival-time upper-mantle tomography and the elusive background mean, *Geophys. J. Int.,* **190**(2), 1271–1278.

Bingen, B. *et al.*, 2005. Timing of continental building in the Sveconorwegian orogen, SW Scandinavia, *Nor. Geol. Tidsskr.,* **85**(1–2), 87–116.

Bingen, B., Andersson, J., Soderlund, U. & Moller, C., 2008. The Mesoproterozoic in the Nordic countries, *Episodes,* **31**(1), 29–34.

Bingen, B., Stein, H.J., Bogaerts, M., Bolle, O. & Mansfeld, J., 2006. Molybdenite Re-Os dating constrains gravitational collapse of the Sveconorwegian orogen, SW Scandinavia, *Lithos,* **87**(3–4), 328–346.

Brooks, C.K., 2011. The East Greenland rifted volcanic margin, *Geol. Surv. Denmark Greenland Bull.,* **24,** 96.

Chiao, L.-Y. & Kuo, B.-Y., 2001. Multiscale seismic tomography, *Geophys. J. Int.,* **145**(2), 517–527.

Cloetingh, S. & Burov, E., 2011. Lithospheric folding and sedimentary basin evolution: a review and analysis of formation mechanisms, *Basin Res.,* **23**(3), 257–290.

Crotwell, H.P. & Owens, T.J., 1999. The TauP toolkit: flexible seismic traveltime and raypath utilities, *Seismol. Res. Lett.,* **70,** 154–160.

Dahlen, F., Hung, S.-H. & Nolet, G., 2000. Fréchet kernels for finite-frequency traveltimes—Theory, I., *Geophys. J. Int.,* **141**(1), 157–174.

Ebbing, J., 2007. Isostatic density modelling explains the missing root of the Scandes, *Norw. J. Geol.,* **87,** 13–20.

Ebbing, J. & Olesen, O., 2005. The Northern and Southern Scandes—structural differences revealed by an analysis of gravity anomalies, the geoid and regional isostasy, *Tectonophysics,* **411**(1–4), 73–87.

Eken, T., Plomerova, J., Roberts, R., Vecsey, L., Babuska, V., Shomali, H. & Bodvarsson, R., 2010. Seismic anisotropy of the mantle lithosphere beneath the Swedish National Seismological Network (SNSN), *Tectonophysics,* **480,** 241–258.

Eken, T., Plomerova, J., Vecsey, L., Babuska, V., Roberts, R., Shomali, H. & Bodvarsson, R., 2012. Effects of seismic anisotropy on *P*-velocity tomography of the Baltic Shield, *Geophys. J. Int.,* **188**(2), 600–612.

Eken, T., Shomali, Z.H., Roberts, R. & Bödvarsson, R., 2007. Upper-mantle structure of the Baltic Shield below the Swedish National Seismological Network (SNSN) resolved by teleseismic tomography, *Geophys. J. Int.,* **169**(2), 617–630.

England, R.W. & Ebbing, J., 2012. Crustal structure of central Norway and Sweden from integrated modelling of teleseismic receiver functions and the gravity anomaly, *Geophys. J. Int.,* **191**(1), 1–11.

Euler, G., 2014. 'Project SEIZMO'. Available at: http://epsc.wustl.edu/~ggeuler/codes/m/seizmo/, last accessed 14 June 2021.

Foulger, G.R. *et al.*, 2013. Caveats on tomographic images, *Terra Nova,* **25**(4), 259–281.

Foulger, G.R. & Pearson, D.G., 2001. Is Iceland underlain by a plume in the lower mantle? Seismology and helium isotopes, *Geophys. J. Int.,* **145**(3), F1–F5.

Frassetto, A. & Thybo, H., 2013. Receiver function analysis of the crust and upper mantle in Fennoscandia—isostatic implications, *Earth planet. Sci. Lett.,* **381,** 234–246.

Gaal, G. & Gorbatschev, R., 1987. An outline of the Precambrian evolution of the Baltic Shield, *Precambrian Res.,* **35,** 15–52.

Gabrielsen, R.H., Inge, J., Pascal, C., Braathen, A., Petter, J., Etzelmuller, B. & Donnell, S.O., 2010. Latest Caledonian to present tectonomorphological development of southern Norway, *Mar. Pet. Geol.,* **27**(3), 709–723.

Gee, D.G., Fossen, H., Henriksen, N. & Higgins, A.K., 2008. From the early Paleozoic platforms of Baltica and Laurentia to the Caledonide orogen of Scandinavia and Greenland, *Episodes,* **31**(1), 44–51.

Gradmann, S., Ebbing, J. & Fullea, J., 2013. Integrated geophysical modelling of a lateral transition zone in the lithospheric mantle under Norway and Sweden, *Geophys. J. Int.,* **194**(3), 1359–1374.

Henriksen, N.E., 2008. *Geological History of Greenland—Four Billion Years of Earth Evolution,* Geological Survey of Denmark and Greenland, 272pp.

Högdahl, K., Andersson, U.B. & Eklund, O., 2004. *The Transscandinavian Igneous Belt (TIB) in Sweden: a Review of Its Character and Evolution,* Special Paper of the Geological Survey of Finland.

Hung, S.H., Chen, W.-P. & Chiao, L.Y., 2011. A data-adaptive, multiscale approach of finite-frequency, traveltime tomography with special reference to P and S wave data from central Tibet, *J. geophys. Res.,* **116,** B06307.

Hung, S.H., Dahlen, F.A. & Nolet, G., 2001. Wavefront healing: a banana-doughnut perspective, *Geophys. J. Int.,* **146**(2), 289–312.

Hung, S.H., Shen, Y. & Chiao, L.Y., 2004. Imaging seismic velocity structure beneath the Iceland hot spot: a finite frequency approach, *J. geophys. Res.,* **109**(B8).1–16.

Husebye, H., Hovland, J., Christoffersson, A., Åström, K., Slunga, R. & Lund, C., 1986. Tomographical mapping of the lithosphere and asthenosphere beneath southern Scandinavia and adjacent areas, *Tectonophysics,* **128,** 229–250.

Japsen, P. & Chalmers, J.A., 2000. Neogene uplift and tectonics around the North Atlantic: overview, *Glob. Planet Change,* **24**(3–4), 165–173.

Kennett, B.L.N., 1995. Seismic traveltime tables, in *Global Earth Physics: A Handbook of Physical Constants,* pp. 126–143, ed. Ahrens, T.J., AGU.

Kennett, B.L.N. & Gudmundsson, O., 1996. Ellipticity corrections for seismic phases, *Geophys. J. Int.,* **127**(1), 40–48.

King, S.D. & Anderson, D.L., 1998. Edge-driven convection, *Earth planet. Sci. Lett.,* **160**(3), 289–296.

Kolstrup, M.L., Hung S.H. & Maupin, V. 2015. Multiscale, finite-frequency P and S tomography of the upper mantle in the southwestern Fennoscandian Shield, *Geophy. J. Int.,* **202,**190–218.

Kolstrup, M.L. & Maupin, V., 2015. Measuring and crust-correcting finite-frequency traveltime residuals-application to southwestern Scandinavia, *Solid Earth,* **6**(4), 1117–1130.

Kraft, H., Thybo, H., Vinnik, L. & Oreshin, S., 2019,. Crustal structure in central-eastern Greenland from receiver functions, *Geophys. J. Int.,* **124,** 1653–1670.

Lahtinen, R., Korja, A. & Nironen, M., 2005. *Paleoproterozoic tectonic evolution. In: Lehtinen, M., Nurmi, P.A., Ramö, O.T. (Eds.) Precambrian Geology of Finland - Key to the Evolution of the Fennoscandian Shield*. Elseiver Science B.V., Amsterdam, 481–532.

Lawver, L. & Müller, R., 1994. Iceland hotspot track, *Geology,* **22,** 311–314.

Levin, V. & Park, J., 1997. *P-SH* conversions in a flat-layered medium with anisotropy of arbitrary orientation, *Geophys. J. Int.,* **131**(2), 253–266.

Lou, X., van der Lee, S. & Lloyd, S., 2013. AIMBAT: a Python/Matplotlib tool for measuring teleseismic arrival time, *Seismol. Res. Lett.,* **84**(1), 85–93.

Makushkina, A., Tauzin, B., Tkalčić, H. & Thybo, H., 2019. The mantle transition zone in Fennoscandia: enigmatic high topography without deep mantle thermal anomaly, *Geophys. Res. Lett.,* **46,** 3652–3662.

Mansour, W.B., England, R.W., Fishwick, S. & Moorkamp, M., 2018. Crustal properties of the northern Scandinavian mountains and Fennoscandian shield from analysis of teleseismic receiver functions, *Geophys. J. Int.,* **214**(1), 386–340.

Marotta, A.M., Bayer, U., Scheck, M. & Thybo, H., 2001. The stress field below the NE German Basin: effects induced by the Alpine collision, *Geophys. J. Int.,* **144,** F8–F12.

Marquart, G. & Schmeling, H., 2004. A dynamic model for the Iceland Plume and the North Atlantic based on tomography and gravity data, *Geophys. J. Int.,* **159**(1), 40–52.

Maupin, V., 2021. Combining asynchronous data sets in regional body-wave tomography, *Geophys. J. Int.,* **224**(1), 401–415.

Maupin, V., Agostini, A., Artemieva, I., Balling, N., Beekman, F., Ebbing, J. & Weidle, C., 2013. The deep structure of the Scandes and its relation to tectonic history and present-day topography, *Tectonophysics,* **602,** 15–37.

Medhus, A.B., Balling, N., Jacobsen, B., Weidle, C., England, R., Kind, R., Thybo, H. & Voss, P., 2012. Upper-mantle structure beneath the Southern Scandes Mountains and the Northern Tornquist Zone revealed by *P*-wave traveltime tomography, *Geophys. J. Int.,* **189**(3), 1315–1334.

Molnar, P. & Houseman, G.A., 2004. The effects of buoyant crust on the gravitational instability of thickened mantle lithosphere at zones of intracontinental convergence, *Geophys. J. Int.,* **158**(3), 1134–1150.

Nielsen, S.B., Gallagher, K., Leighton, C., Balling, N., Svenningsen, L., Jacobsen, B.H. & Lykke-Andersen, H., 2009. The evolution of western Scandinavian topography: a review of Neogene uplift versus the ICE (isostasy-climate-erosion) hypothesis, *J. Geodyn.,* **47**(2–3), 72–95.

Parnell-Turner, R., White, N., Henstock, T., Murton, B., Maclennan, J. & Jones, S., 2014. A continuous 55-million-year record of transient mantle plume activity beneath Iceland, *Nat. Geosci.,* **7,** 914–919.

Pedersen, H.A., Debayle, E., Maupin, V., Kozlovskaya, E., Jämsen, T., Silvennoinen, H. & Volosov, S., 2013. Strong lateral variations of lithospheric mantle beneath cratons—example from the Baltic Shield, *Earth planet. Sci. Lett.,* **383,** 164–172.

Pedersen, V.K., Huismans, R.S. & Moucha, R., 2016. Isostatic and dynamic support of high topography on a North Atlantic passive margin, *Earth planet. Sci. Lett.,* **446,** 1–9.

Rickers, F., Fichtner, A. & Trampert, J., 2013. The Iceland-Jan Mayen plume system and its impact on mantle dynamics in the North Atlantic region: evidence from full-waveform inversion, *Earth planet. Sci. Lett.,* **367,** 39–51.

Sandoval, S., Kissling, E. & Ansorge, J., 2004. High resolution body wave tomography beneath the SVEKALAPKO array—II. Anomalous upper mantle structure beneath the central Baltic Shield, *Geophys. J. Int.,* **157**(1), 200–214.

Sandrin, A. & Thybo, H., 2008. Deep seismic investigation of crustal extensional structures in the Danish Basin along the ESTRID-2 profile, *Geophys. J. Int.,* **173,** 623–641.

Schoonman, C.M., White, N.J. & Pritchard, D., 2017. Radial viscous fingering of hot asthenosphere within the Icelandic plume beneath the North Atlantic Ocean, *Earth planet. Sci. Lett.,* **468,** 51–61.

Shomali, Z.H. & Roberts, R.G. the TORWorking Group, 2002. Non-linear body wave teleseismic tomography along the TOR array, *Geophys. J. Int.,* **148,** 562–575.

Silvennoinen, H., Kozlovskaya, E. & Kissling, E., 2016. POLENET/LAPNET teleseismic P wave traveltime tomography model of the upper mantle beneath northern Fennoscandia, *Solid Earth,* **7**(2), 425–439.

Simmons, N.A., Myers, S.C., Morency, C., Chiang, A. & Knapp, D.R., 2021. SPiRaL: a multiresolution global tomography model of seismic wave speeds and radial anisotropy variations in the crust and mantle. *Geophys. J. Int.,* **227**(2), 1366–1391.

Stratford, W., Thybo, H., Faleide, J.I., Olesen, O. & Tryggvason, A., 2009. New Moho map for onshore southern Norway, *Geophys. J. Int.,* **178**(3), 1755–1765.

Surlyk, F., 2003. The Jurassic of East Greenland: a sedimentary record of thermal subsidence, onset and culmination of rifting, *GEUS Bull.,* **1,** 657–722.

Thybo, H., 2001. Crustal structure along the EGT profile across the Tornquist Fan interpreted from seismic, gravity and magnetic data, *Tectonophysics,* **334**(3–4), 155–190.

Thybo, H., *et al.* 2021. ScanArray—a broadband seismological experiment in the Baltic Shield, *Seismol. Res. Lett.,* **92,** 2811–2823.

Thybo, H., Heikkinen, P. & Kukkonen, I., 2012. Deep seismic probing of continental crust and mantle, *Tectonophysics,* **508**(1–4), 1–5.

Torsvik, T. *et al.*, 2015. Continental crust beneath southeast Iceland, *Proc. Natl. Acad. Sci. USA,* **112,** E1818–E1827.

Torsvik, T.H., Smethurst, M.A., Meert, J.G., Van Der Voo, R., McKerrow, W.S., Brasier, M.D. & Walderhaug, H.J., 1996. Continental break-up and collision in the Neoproterozoic and Palaeozoic - A tale of Baltica and Laurentia, *Earth-Sci. Rev.,* **40**(3–4), 229–258.

VanDecar, J.C. & Crosson, R., 1990. Determination of teleseismic relative phase arrival times using multi-channel cross-correlation and least squares, *Bull. seism. Soc. Am.,* **80**(1), 150–169.

Weidle, C. & Maupin, V., 2008. An upper-mantle *S*-wave velocity model for Northern Europe from Love and Rayleigh group velocities, *Geophys. J. Int.,* **175,** 1154–1168.

Wessel, P., Smith, W.H., Scharroo, R., Luis, J. & Wobbe, F., 2013. Generic Mapping Tools: improved version released, *EOS, Trans. Am. geophys Un.,* **94,** 409–410.

Winchester, J.A., the PACE TMR Network Team,2002. Palaeozoic amalgamation of Central Europe: new results from recent geological and geophysical investigations, Tectonophysics, **306,** 5–21.

Youssof, M., Thybo, H., Artemieva, I.M. & Levander, A., 2015. Upper mantle structure beneath southern African cratons from seismic finite-frequency *P*- and *S*-body wave tomography, *Earth planet. Sci. Lett.,* **420,** 174–186.

Zhu, H., Bozdağ, E. & Tromp, J., 2015. Seismic structure of the European upper mantle based on adjoint tomography, *Geophys. J. Int.,* **201**(1), 18–52.

Ziegler, P.A. & Cloetingh, S., 2004. Dynamic processes controlling evolution of rifted basins, *Earth-Sci. Rev.,* **64**(1–2), 1–50.

SUPPORTING INFORMATION

Supplementary data are available at *GJI* online.

Figure S1. *P*-wave velocity model in map views for consecutive thirty-two depth slices gathered from the inversion at depths between 50 and 800 km. Grey lines are the national borders.

Figure S2. Geological formations overlaid on the tomography results for the eight shallower depth slices. The −2000 m bathymetry contour with a thin solid line roughly represents the outer margin of the Vøring Plateau. BT: Bergslagen terrane. STZ: Sorgenfrei-Tornquist Zone. TIB: Transscandinavian Igneous Belt. CD: Caledonian cover. SN: Sveconorwegian. LGB: Lapland Granulite Belt.

Figure S3. Inversion of the synthetic 32 layers from checkerboard tests with box sizes 150 × 150 × 150 km^3. The results on the depth slices remaining in between two checker boxes are deteriorated.

Figure S4. Inversion of the synthetic 32 layers from checkerboard tests with box sizes 300 × 300 × 200 km^3. The results on the depth slices remaining in between two checker boxes are deteriorated.

Please note: Oxford University Press is not responsible for the content or functionality of any supporting materials supplied by the authors. Any queries (other than missing material) should be directed to the corresponding author for the paper.